Received: 27 December 2023 | Revised: 11 September 2024 | Accepted: 17 September 2024

DOI: 10.1002/esp.6002

CASE STUDY

ESPL WILEY

PS-InSAR post-processing for assessing the spatio-temporal differential kinematics of complex landslide systems: A case study of DeBeque Canyon Landslide (Colorado, USA)

Marta Zocchi[1] | Michele Delchiaro[1] | Francesco Troiani[1,2] | Gabriele Scarascia Mugnozza[1,2] | Paolo Mazzanti[1,2]

[1]Department of Earth Sciences, SAPIENZA University of Rome, Rome, Italy

[2]CERI Research Centre on Geological Risks, Sapienza University of Rome, Rome, Italy

Correspondence
Marta Zocchi and Michele Delchiaro, Department of Earth Sciences, SAPIENZA University of Rome, 00185 Rome, Italy.
Email: marta.zocchi@uniroma1.it and michele.delchiaro@uniroma1.it

Abstract

The complex superimposition of different kinematics and nested sectors within landslide systems amplifies the challenge of interpreting their heterogeneous displacement pattern and targeting effective mitigation solutions. As an example of such peculiar spatio-temporal behaviour, the DeBeque Canyon Landslide (Colorado, USA) is emblematic of the application of interferometric post-processing analysis for a detailed, remotely-based investigation. We employed a multi-geometry Persistent Scatterers (PS) InSAR dataset to provide continuous information on the spatio-temporal scale and achieve a solid representation of the segmented kinematics and timings. Using an updated geomorphological map of the landslide system, we performed a two-dimensional decomposition of the Persistent Scatterers (PS) dataset to determine the displacement orientation and inclination for each internal sector of the landslide system. We then conducted statistical analyses on the displacement vector characteristics and time series data. These analyses enabled us to spatially characterize the segmented activity patterns of the landslide system and identify abrupt changes in trends associated with preparatory and triggering factors. A clear differentiation of the rotational or translational kinematics within the landslide system was accomplished solely using surface displacement measures. Moreover, the application of a Bayesian model on the bi-dimensional vector time series leads to the identification of significant differences in the deformational behaviour of each sector with respect to precipitation and temperature factors. Our approach represents a replicable method for local-scale characterization and monitoring of landslides exhibiting complex spatio-temporal displacement patterns and providing an effective, low-cost solution for transportation agencies from a risk-reduction perspective.

KEYWORDS
InSAR post-processing, landslide kinematics, landslide system, multi-geometry combination, PS-InSAR, time series decomposition

1 | INTRODUCTION

Landslides significantly impact mountain environments worldwide, reshaping the topography but also affecting human activities, thus posing a threat to urban settlements (Agliardi et al., 2012; Bozzano et al., 2010; Crosta et al., 2013; Herrera et al., 2018; Raspini et al., 2017). The interplay of litho-structural factors and hydro-climatic, conditions controls their differential erosion and sediment redistribution, affecting the long-term morphoevolution of the slopes (Crosta et al., 2017; Delchiaro et al., 2019, 2023, 2024; Della Seta

et al., 2017; Marmoni et al., 2023; Preisig et al., 2016; Riva et al., 2018). Under the ongoing effect of such factors, rock masses accumulate stress and experience a slow yet persistent deformation, which may result in complex spatiotemporal arrangements of landslides, derived from the internal segmentation and mobilization of nested bodies (Lopez Saez et al., 2012) or the superimpositions of different types of movements (Bossi et al., 2015; Valiante et al., 2016; Wang et al., 2020). The term landslide system (Valiante et al., 2021 and references therein) describes such arrangements of gravity-driven morphotypes derived, over the long term, from the same slope deformation. Assessing this segmentation through an extensive spatial kinematic characterization, including the quantification of distinct displacement rates and mechanisms, as well as the identification of nested bodies and secondary failures, is crucial for understanding the complex morphodynamics of these phenomena (Bigot-Cormier et al., 2005; Crosta et al., 2017; Delchiaro et al., 2023, 2024; Dong et al., 2023; El Bedoui et al., 2009; Frattini et al., 2018).

The factors controlling landslide system history can be long-term static, as in the case of predisposing ones (e.g., bedding, lithology), or dynamic as in the case of the preparatory ones (e.g., temperature, river incision, glacial debuttressing). In addition, short-term triggering factors (e.g., earthquakes and extreme rainfall events) can lead the slope to the ultimate failure. In this regard, precipitation events play a decisive role both in the short term, acting as triggers when heavy rainfall or sudden snowmelt occurs (Crosta et al., 2014; Del Ventisette et al., 2012; Grøneng et al., 2011; Nishii et al., 2013) and, along with temperature, as preparatory factors, whenever prolonged rainfalls and seasonal changes undermine the slope marginal stability over the mid- and long-term (Ibsen & Casagli, 2004; Popescu, 2002; Scheevel et al., 2017; Steger et al., 2022). The interplay between the aforementioned factors impacts the temporal displacement evolution and may lead to the differential reactivation of the landslide system's internal sectors and even to a generalized failure (Del Ventisette et al., 2012; Wang et al., 2020). From a geotechnical perspective, mitigation measures planning and construction become challenging due to the high spatio-temporal displacement variability, especially when strategic infrastructures are involved. An overall analysis is often carried out through traditional geotechnical and geophysical techniques that allow acquiring accurate localized measurements (Crosta & Agliardi, 2002). However, given their spot-like peculiarity and the high cost of pervasive positioning, they fail to provide a comprehensive perception of the heterogeneous displacement pattern of the landslide, likely underestimating the actual fragmentation of the system.

To achieve a robust yet persistent interpretation of the spatio-temporal evolution of landslide systems, Interferometric Synthetic Aperture Radar (InSAR) and Light Detection and Ranging (LiDAR) can be effectively employed for a thorough investigation as they provide high spatio-temporal resolution, and extensive measurement coverage (Ciampalini et al., 2016; Gischig et al., 2011; Singhroy & Molch, 2004; Vick et al., 2020; Xu et al., 2021). Combining these two techniques is ideal for investigating slow-moving phenomena in mountainous and hilly terrains. Whereas LiDAR data in the form of Digital Elevation Models (DEMs) are often employed for a detailed morphometric characterization of landslide signatures on rugged topography (Ardizzone et al., 2007; Glenn et al., 2006; Jaboyedoff et al., 2012; Kasai et al., 2009), InSAR techniques proved optimal detection of subtle ground deformations moving within the specific sensor's detection capability (i.e., from several centimetres to a few millimetres per year) (Mazzanti et al., 2015; Wasowski & Bovenga, 2014). From the traditional differential interferometry method (Crippa et al., 2020; Dong et al., 2018; Reyes-Carmona et al., 2023; Tarchi et al., 2003) to advanced multi-temporal methodologies based on Small Baseline Subsets (Berardino et al., 2002) and Persistent Scatterers - PS (Moretto et al., 2021), InSAR-derived displacements are essential for the landslide's deformational pattern quantification and mapping purposes (Antonielli et al., 2019; Bonì et al., 2020; Bordoni et al., 2018; Bozzano et al., 2017; Di Martire et al., 2017). The PS-InSAR technique has found widespread application in analysing the spatial displacement patterns associated with slow deformation processes, providing valuable insights for investigating landslide systems' segmented and heterogeneous kinematic behaviour (Crippa & Agliardi, 2021) and considering their interaction with man-made structures (Frattini et al., 2013). In addition, PS displacement time series can be correlated with external meteorological forcings. In this case, examining the historical temporal deformation pattern of the slope process can allow us to highlight the relationship between reactivations and sudden accelerations in the displacement trend, triggered by high-intensity, short-duration events or influenced by medium and long-term seasonal trends.

Nevertheless, the motion assessment through PS-InSAR applications is heavily affected by the intrinsic characteristics of the technique, which retrieves the ground deformation velocity along the satellite line-of-sight (LOS) and therefore fails to record the real tridimensional components of the displacement vector (Crippa et al., 2021; Eriksen et al., 2017). Moreover, considering the complexity of examining multiple deforming sectors nested in a larger disrupted rock mass, the present literature still offers rare studies that aim to address this challenge in the spatial domain (Crippa et al., 2021; Eriksen et al., 2017) and, to the best of the authors' knowledge, none in the temporal one. Crippa et al. (2021) quantified the landslide internal heterogeneity for regional-scale classification purposes implying the necessity of embracing a more generalized assumption when considering landslide segmentation across extensive areas. Conversely, Eriksen et al. (2017) exploited the vectorial decomposition for identifying complex deformations displacement patterns at the local scale yet avoiding proposing a detailed internal subdivision of the processes constituting the landslide system. Therefore, this study aims to utilize PS-InSAR analysis to investigate the spatial kinematic variability and temporal dynamics of a landslide system, while also considering the potential influence of triggering and preparatory factors. The novelty of our work lies in the development and application of versatile post-processing techniques, which enable a comprehensive exploration of spatio-temporal deformation dynamics from a remote sensing perspective. This methodology proves particularly valuable in scenarios where field data are limited or unavailable, offering a robust alternative for landslide monitoring and analysis. The first part of the methodological section is dedicated to the description of the exemplary case study used in the present work. Then, we described how we estimated the two-dimensional displacement vector and employed it as an alternative to the LOS velocity for further displacement analysis. We used the combination of the multi-geometry Sentinel-1 dataset acquired between 2014 and 2019 considering it with respect to the LiDAR-derived local topography to derive the bidimensional vector. The spatial and temporal outcomes

of the InSAR post-processing analysis are described in the two main subsections of the results. First, we delineated the spatial deformation pattern of the selected landslide exploiting the decomposed displacement vector to obtain a clear distinction of the peculiar kinematics of each sector composing the system. Eventually, from a temporal point of view, we correlated the decomposed velocity to the meteo-climatic data, identifying a correlation between displacement acceleration phases and precipitation and temperature factors, acting both as triggering and preparatory.

2 | MATERIALS AND METHODS

The methodology presented in the current section is tailored to investigate the spatial variability and morphodynamic evolution of the DeBeque Canyon Landslide system, described in Section 2.1. This system was used as an exemplary test site to investigate the heterogeneous deformational behaviour of a slow-deforming slope threatening Interstate 70, one of the major highways of the United States. Detailed mapping of the geomorphological features of the landslide was carried out through visual interpretation of a high-resolution digital topographic model (Section 2.2) as a preliminary step for further quantitative investigation on a multi-geometry interferometric dataset (Section 2.3). We differentiated the heterogeneous spatial pattern by considering, in the first place, the decomposed velocity vector distribution over the landslide's sectors. Subsequently, we also examined the vector's time series for each zone of the landslide to retrieve specific timings and correlations with preparatory and triggering factors.

2.1 | The DeBeque canyon case study

The study area is located in the northern part of Mesa County in Colorado (USA): here, channelized surficial waters belonging to the Colorado River system represent the main morphogenetic agent, incising the extensive plateau in the form of deep canyons and playing a crucial role in disrupting the slope stability along its banks (Figure 1). A critical example of this interaction is the DeBeque Canyon Landslide (DCL) at milepost 51 of Interstate 70, a landslide system that has historically impacted the road, thus representing an area of concern for the Colorado Geological Survey (White et al., 2003).

This test site is in the western portion of the Upper Colorado River Basin, which is characterized by an arid to semi-arid climate (Kopytkovskiy et al., 2015) and can be referred to as BSk based on the Köppen climate classification (Zepner et al., 2020). Summers are typically hot and dry, with temperatures reaching an average of 26°C in July, while winters are cold, with an average temperature below 0°C in December–January, as represented in the climate chart reported in Figure 1. Precipitations are scarce, averaging around 235 mm per year (Figure 1). The annual temperature range is very high, with values ranging from 20.3 to 30.7°C. The highest temperatures are recorded at low elevations, in the Colorado Basin, where the landslide is located. Future projections of climatic trends draw attention to the progressive increase of drought periods, where liquid and solid precipitation are likely to decline while temperatures are expected to increase 2–4°C (Ficklin et al., 2013; Kopytkovskiy et al., 2015). Such temperature increase is linked with the anticipation of snowmelt and runoff timing during Spring, thus potentially influencing the deformational trend of mass movements in the area (Ficklin et al., 2013).

Historically referred to as the "Tunnel Landslide", the DCL showed first signs of activity before 1910 (the precise date is unknown), when a 300 m-long, 90 m-high sandstone slab partially dammed the Colorado River that deviated its path towards the opposite bank (White et al., 2003). Two other historic paroxysmal events were recorded before the last catastrophic failure occurred in April 1998. As reported by White (2005), the landslide movement caused the permanent diversion of the Colorado River channel and the Old Highway 6 destruction in 1924, which was subsequently relocated but disrupted again in 1958. The last paroxysmal failure occurred in April 1998: a section of the newly built Interstate 70, located at the foot of the landslide, was laterally shifted 3 m and pushed up around 7 m. Ongoing displacement of these sectors is currently recorded and monitored by the Colorado Department of Transportation and Colorado Geological Survey using in-situ instruments and repeated LiDAR scanning (Gaffney et al., 2002; Weidner & Walton, 2020; White, 2014).

The first conceptual model of the geology, subsurface geometry and the interaction of the different failure mechanisms involved in the DCL system was proposed by White (2000) and White et al. (2003), who reconstructed the model by means of a photogrammetric study based on aerial stereo-pairs available for the landslide site. Field mapping and wire-line core borings were also performed to reconstruct structural and stratigraphical information. The deformational area is divided into three main sectors (Figure 2) based on the surficial expression of the distinct failure mechanisms affecting the slope, namely the Upper Block, Rubble Zone and West Disturbed Block (Weidner & Walton, 2020; White, 2000; White et al., 2003).

The Upper Block is a wedge-shaped block delimited by an active cliff face on the right side and by a set of fractures and tension cracks, part of a shear zone along the upper side, which promotes its sliding. The material supplied by the retreating cliff accumulates in the Rubble Zone, where it translates to the rotational area located at the toe of the landslide system (Figure 3a), thus constituting the "Rotational Failure Engine" model proposed by White et al. (2003). Eventually, the West Disturbed Block represents a transitional sector that undergoes both the creep movements of the above Upper Block and the lateral shifting of the main rotational area of the Rubble Zone (Figure 3a) (Weidner & Walton, 2020).

The geology of the DeBeque Canyon, located in the depositional basin of the Colorado Plateau, consists of the upper Mesa Verde Group, a Late Cretaceous sedimentary sequence. This sequence was deposited in a coastal plain environment and is mainly composed of nearly horizontal interbedded layers reflecting the sea level oscillations during the transgressive and regressive cycles of the western Cretaceous Seaway shoreline (Hettinger & Kirschbaum, 2002).

The lithological alternation of prominent massive sandstone beds (up to 30 m) interbedded with less competent, thinner shale and siltstone layers (Gaffney et al., 2002; Weidner & Walton, 2020; White et al., 2003) gives the slope its peculiar step-like morphology. As reported by White et al. (2003), the stability of the DCL system appears to be significantly conditioned by the different geomechanical properties of the less competent layers overlying the sandstone bed

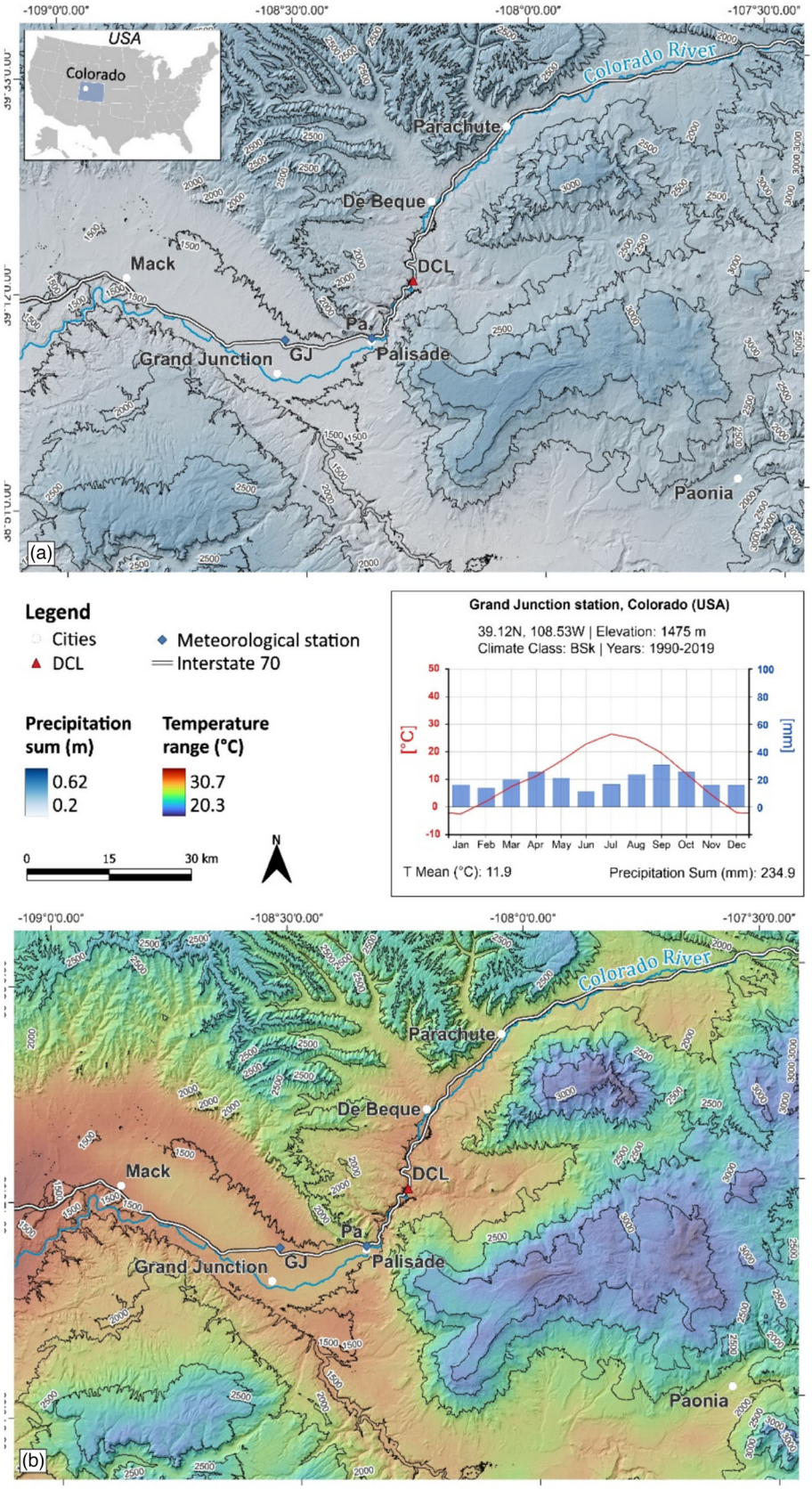

FIGURE 1 Geographical setting of the study area. The map shows the sum of the average annual rainfall (a) and annual temperature range (b) for the western portion of the Colorado basin (Fick & Hijmans, 2017), where the DeBeque Canyon Landslide (red triangle) is located. A representative climate chart is available for the GJ station, the closest station to the study area (Zepner et al., 2020).

outcropping in the proximity of Interstate 70. Figure 3b shows the geological section from the Upper Block, intensely disrupted by a set of vertical fractures, through the Rubble Zone (characterized by a translative component of the deformations) and eventually to the Main Rotational Zone. Moreover, a fault running parallel to the headscarp contributes to compromising the rock mass stability (White et al., 2003).

2.2 | Terrain visual analysis

In this study, terrain analyses were carried out using a Digital Terrain Model (DTM) with a ground resolution equal to 1 m derived from a LiDAR survey performed within the framework of the 3D Elevation Program (3DEP). This program provides freely downloadable bare-earth models over the United States territories (U.S. Geological

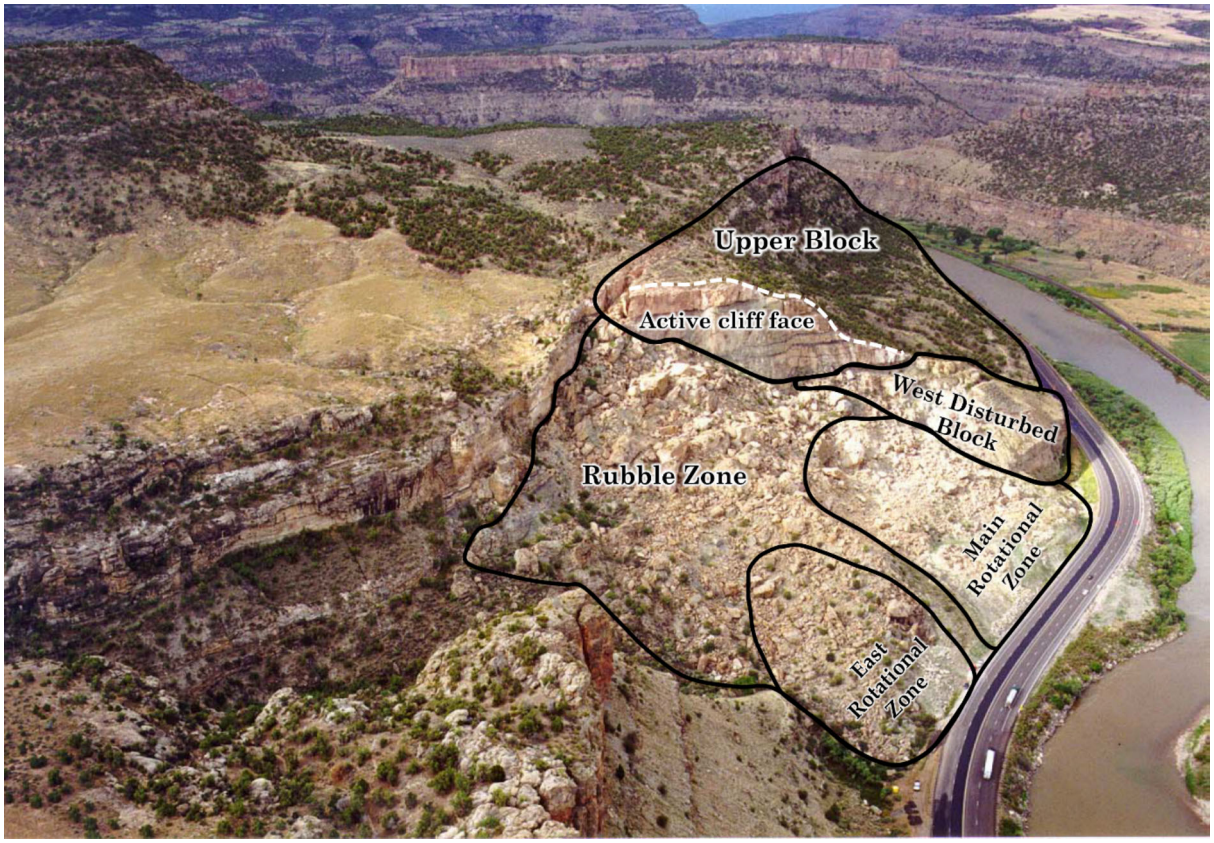

FIGURE 2 Oblique aerial view of the DCL (photo taken pointing to the west direction). The landslide system is divided into different sectors, each one characterized by distinct kinematics (modified after White et al., 2003).

Survey, 2019). The DTM used for our study area was derived in 2016. Preliminary recognition and mapping of the landforms and processes occurring along the slope were supported by the visual interpretation of hillshade maps, realized with varying sun azimuth angles and 1 m and 5 m intervals contour lines maps, both of which were extracted using the geomorphological tools available in the QGIS 3.22 software. In addition to the DTM interpretation, freely available GoogleEarth images (GoogleEarth Pro, 2016) supported the visual recognition of the main landslide characteristics (e.g., primary and secondary scarps, reverse slopes, convex foot, surficial drainage modifications) that are clear evidence of a disrupted rock mass.

2.3 | InSAR analysis

The quantification of the deformational motion occurring along the slope of interest has been performed through an Advanced Differential Interferometric SAR analysis (A-DInSAR). Specifically, we used the Persistent Scatterers Interferometry approach (Ferretti et al., 2001), one of the most common multi-temporal processing methods. The assessment of surficial deformations is based on the information achieved by high-coherent pixels of every acquired SAR image (Kampes, 2006). The fundamental improvement of this procedure is that for each high-stability pixel, called Persistent Scatterer (PS) after Ferretti et al. (2000) and Ferretti et al. (2001), the atmospheric contribution can be precisely estimated and removed, thus reducing both spatial and temporal decorrelation issues (Mazzanti et al., 2021; Moretto et al., 2021). The dataset analysed in the SARPROZ (the SAR processing tool by Perez) software (Perissin et al., 2011) includes 129 ascending and descending Sentinel-1 imagery, spanning the 2014–2018 time interval.

The processing allowed us to estimate the average LOS velocity and the displacement time series for more than 3,000 PS over the entire landslide area.

The aim of the post-processing step consisted of the in-depth characterization of the DCL system's spatio-temporal evolution. It is necessary to deepen the manipulation of the interferometric data since the display of the LOS mean velocity and its spatialization alone can offer a preliminary, partial insight.

A preliminary evaluation of the radar sensor's capability for recording displacements is decisive for assessing the ground displacement morphodynamics. Since the displacement recorded by the SAR sensor is the unidimensional average velocity (and displacement time series) along the satellite LOS projection, the actual tridimensional movement of the landslide is considerably underestimated or else, in the most unfavourable scenario, not detectable should the motion occur orthogonally to the satellite LOS.

Through the C-factor computation, we can represent the percentage of ground displacement that can be recorded along the slope, taking into account both the radar signal characteristics and the terrain site-specific morphology (Notti et al., 2014).

It is calculated as follows:

$$C = \left[N \cdot \cos(S) \cdot \sin\left(A - \frac{\pi}{2}\right)\right] + \left[E \cdot \left(-1 \cdot \cos(S) \cdot \left(\cos\left(A - \frac{\pi}{2}\right)\right) + (H \cdot \sin(S))\right)\right] \quad (1)$$

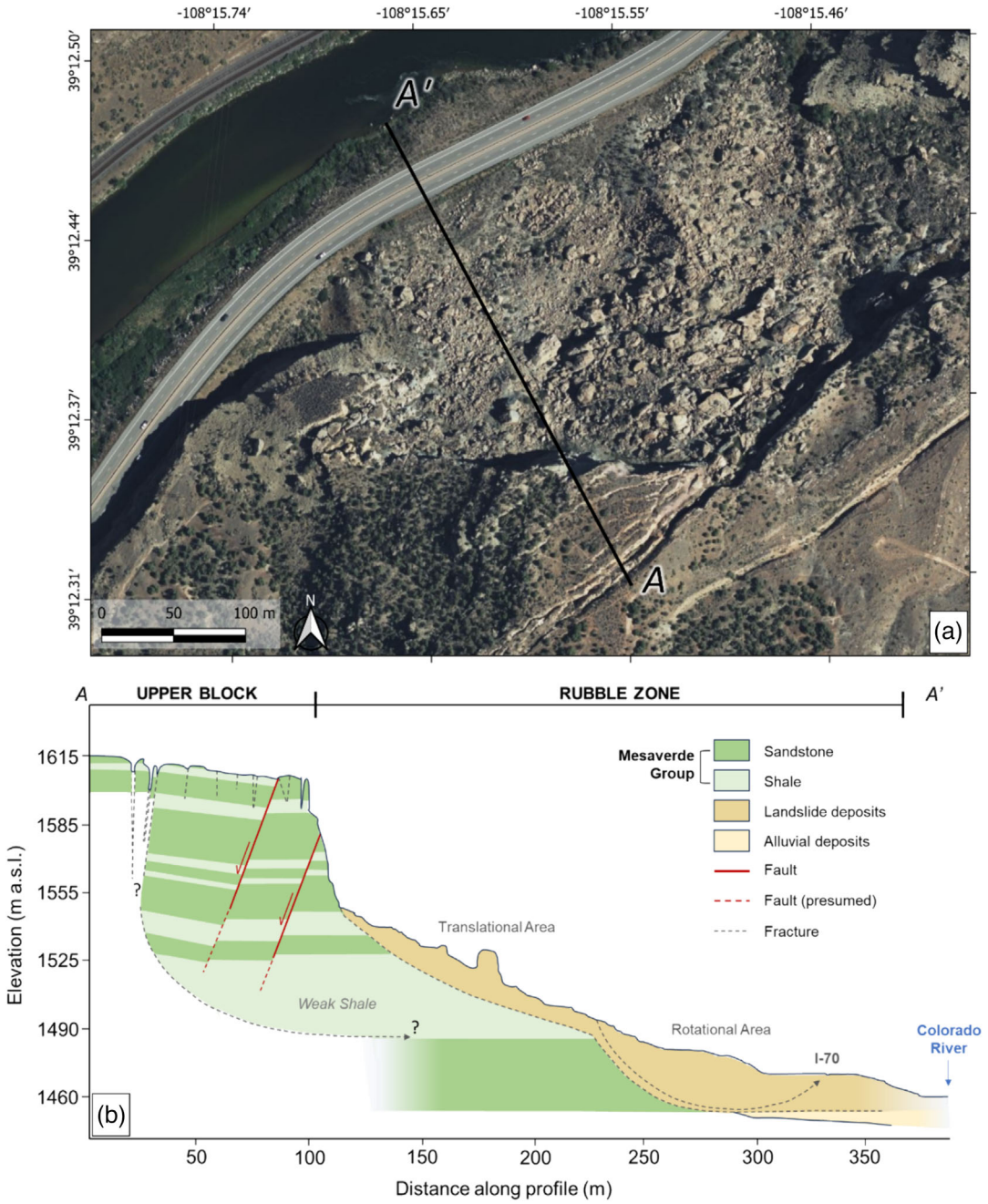

FIGURE 3 Satellite image of the DeBeque canyon landslide (Bing satellite basemap, available on QGIS 3.22) with an overlay of the geological cross-section (panel a). Panel b illustrates the AA' geological cross-section of the western part of the landslide (modified after White et al., 2003).

where:

$$N = \cos\left(\frac{\pi}{2} - \alpha\right) * \cos(\pi - \theta)$$

$$E = \cos\left(\frac{\pi}{2} - \alpha\right) * \cos\left(\frac{3}{2}\pi - \theta\right)$$

$$H = \cos(\alpha)$$

SAR orbital parameters are represented by the LOS velocity angles for the vertical, North and East directions (namely H, N and E) and azimuth (θ) and incidence (α) angles, while S and A represent the slope and aspect derived from the DEM. Every parameter is expressed in radians.

Starting from the combination of the ascending and descending PS datasets, we resolved the displacement vectors along the horizontal (East–West, Vh) and vertical (Up-Down, Vv) directions (Notti et al., 2014; Raspini et al., 2017; Tofani et al., 2013) (Figure 4). By combining ascending and descending InSAR data, we extract the vertical and east–west (E-W) displacement components. These directions offer the most retrievable information due to the reduced sensitivity of SAR sensors in the north–south (N-S) direction, intrinsic in the side-looking perspective of the satellite. Decomposition along other directions, such as southeast-northwest (SE-NW), which aligns with the predominant movement of most landslide sectors, would result in further underestimation of the decomposed velocities. Consequently, this would introduce limitations in the interpretation of landslide behaviour. To perform the vectorial decomposition, two distinct layers

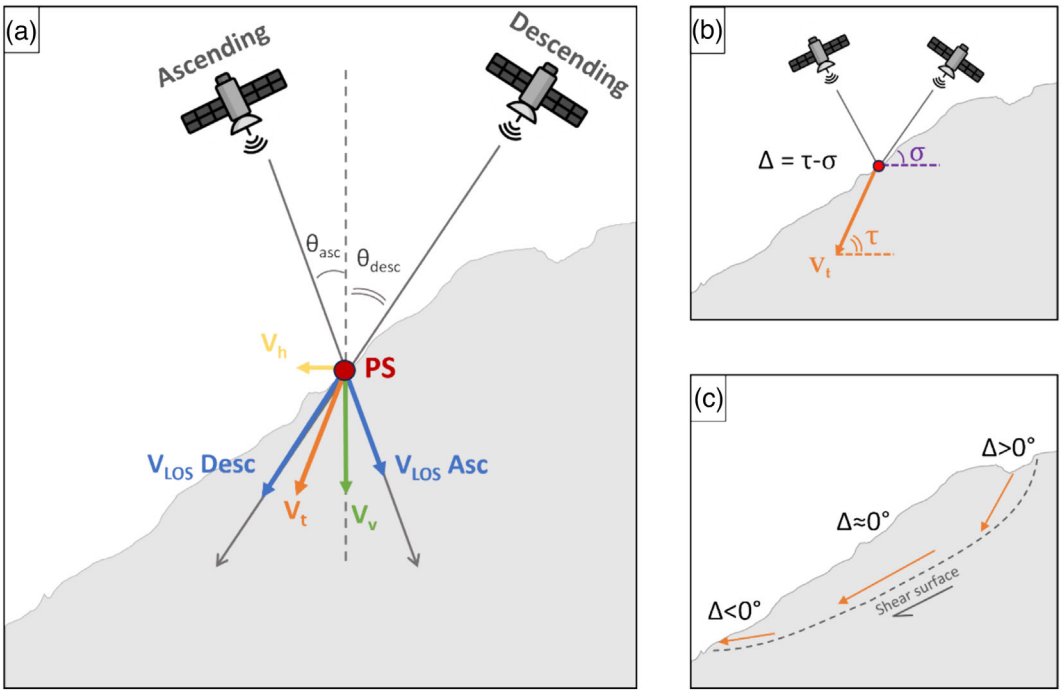

FIGURE 4 Schematic representation of the decomposed radar signal starting from the two LOS velocities (blue arrows) along the ascending and descending orbits. The vertical and horizontal components of the movement are represented in yellow and green, respectively, while the resultant Vt vector is displayed in orange. Relating Vt inclination (τ) to the local slope (σ) as a difference, the local Δ gradient, indicating landslide displacement direction, is retrieved (panel b). Negative values show "out" of slope movement (bulging), positive values show "into" slope movement (subsidence) and Δ ≈ 0 indicates displacement parallel to the slope (translative movement) (panel c).

for both geometries and their respective orbit parameters (i.e., heading and incidence angles) are needed as input data. The PS are then spatially joined based on the geometric distance between neighbours and resampled into synthetic points distributed on a regular grid. Considering the ground resolution of Sentinel-1 data, we set the cell size equal to 15 m to avoid misrepresenting the effective vector motion and to avoid incorporating the contribution of PS too distant from each other. The final multi-look combination output consists of two separate layers of synthetic points regularly distributed over the study area, representing the derived Vh and Vv components.

Moreover, for each synthetic PS, we obtained the bidimensional vector Vt (Figure 4a), resulting from the combination of the decomposed velocity in the up-down and east–west directions according to the following formula:

$$Vt = \sqrt{Vh^2 + Vv^2} \quad (2)$$

Its respective angle τ, was also derived as:

$$\tau = cos^{-1}(Vh/Vt) \quad (3)$$

and it represents the detected displacement gradient of the investigated phenomenon. Relating τ to the local slope as a difference (τ-σ, Figure 4b), we extrapolated the local Δ gradient, which indicates the landslide's displacement direction with respect to the slope (Figure 4c): negative values describe a displacement "out" of the slope (bulging), while positive values indicate a movement "into" the slope (subsidence). When Δ approximates to 0 (τ = slope), the landslide displacement occurs along the slope (translative movement) (Figure 4c). The progressive shift from translational to rotational dynamics can be evaluated by analysing the statistical distribution of the Δ gradient on the different zones (Crippa et al., 2021). Furthermore, the differential DCL system kinematics were examined by projecting the vector Vt along profiles that intersected the most significant geomorphological elements.

The PS displacement time series has been utilized to assess the style of activity of the landslide and gain insights into the process of temporal evolution considering its response to potential triggering and preparatory factors (i.e., precipitations and temperature variations).

For this purpose, time series displacement for the 2014–2018 period was examined using the Bayesian Estimator of Abrupt change, Seasonality and Trend (BEAST) analysis package (Zhao et al., 2019). We opted to use it because it exploits the scheme known as Bayesian model averaging (BMA), a category of multi-model techniques broadly called ensemble learning. Indeed, inconsistent or contradicting insights gained from different models are a common problem of the single-best-model paradigm. Unlike conventional criterion-based methods that choose only a single best model, the Bayesian ensemble algorithmic paradigm can embrace all candidate models, evaluate how probable each of them is to be a true model and synthesize the many models into an average model. According to the BEAST time series decomposition, a time series $D = \{t_i, y_i\}_{i=1,\ldots,n}$ is composed of three components—seasonality S, trend T and noise ϵ - where y is the displacement, t is the time from the observed data at n points of time, that can be formulated as follows:

$$y_i = S(t_i;\Theta_s) + T(t_i;\Theta_T) + \epsilon_i \quad (4)$$

where abrupt changes (i.e., changepoints, cp) are implicitly encoded in the parameters Θ_s and Θ_T of the seasonal and trend signals. Then, a general linear model to parameterize S(·) and T(·) is adopted (Jiang et al., 2010; Verbesselt et al., 2010). In such formulation, the noise ε is assumed to be Gaussian with a magnitude of σ, capturing the remainder in the data not explained by the seasonal S(·) and trend T(·) signals. We focused on the BEAST output estimates of the trend's abrupt changes and their associated probabilities of occurrence, which were assumed to be representative of authentic variations in the temporal displacement series. In our analysis, the output consisted of a set of variables related to changepoints and their corresponding probabilities of representing authentic variations in the temporal displacement pattern.

The landslide motion retrieved from the vector Vt was analysed alongside liquid precipitation and temperature data recorded by the Palisade station (Colorado Climate Center, n.d.) located in the homonymous city (Figure 1). This station was selected as the nearest and most complete source for comparing displacement with local climatic conditions. However, only liquid precipitation data was used, as the snow data for the study area, also available from the Palisade station, was significantly incomplete and fragmented, preventing its use as a reliable variable for the analysis.

The comparison of meteo-climatic and displacement datasets was conducted on two different timescales for each internal sector of the landslide and eventually to highlight differing geomechanical responses to the same predisposing and triggering factors. First, the meteorological and PS recorded movements were aggregated on weekly timesteps to assess subtle variations in the limited temporal interval covered by the interferometric analysis. Moreover, the climatic control on the rock mass was also evaluated extending the investigated period, spanning several decades and available for the Grand Junction weather station (Figure 1) (Zepner et al., 2020). We thus considered the averaged rainfall and temperature values over the past 30 years to address the influence of the climate's long-period impact and identify potential changing trends.

3 | RESULTS

The present section describes the results obtained after the visual terrain analysis targeted to map the landslide's features (Section 3.1). Outcomes derived from the spatial and temporal PS-InSAR post-processing are examined in Section 3.2.

3.1 | Geomorphological mapping

Building upon the sector division proposed by White et al. (2003), we refined the landslide characterization through visual interpretation of optical images and high-resolution DTM. This approach was fundamental in identifying additional morphotypes specific to each landslide sector, enhancing the pre-existing interpretation. Figure 5 depicts a few examples of the mapped features, from a general overview of the entire system (Figure 5a) to specific portions of the Rubble Zone (Figure 5b), West Disturbed Block (Figure 5c) and Upper Block fissures and trenches (Figure 5d). As reported in Figure 6, we defined the actual delimitation of each internal sector, modifying the overall extent of the landslide body already mapped by previous authors. One of the most significant changes includes the precise delimitation of the Upper Block zone of influence, whose western border had so far been underestimated or drawn as an uncertain limit (Weidner & Walton, 2020; White et al., 2003). Furthermore, the surficial geomorphological evidence of the disruption was also corroborated by the satellite SAR measurements, which captured movements in an area previously overlooked. This interpretation enabled the expansion of the Upper Block area (Figure 6), influenced by an ongoing and persistent deformation. Right above the landslide crown, two shaded linear features were also recognized from DTM and defined as a retrogressive scarp and a fracture. Their positioning reveals the active displacement of this part of the slope, where PS are scarce or cannot register any movements and corresponds to the retrogressive evolution of the slope instability.

3.2 | InSAR analysis

Figure 7 presents the mean C-factor values for each internal sector of the DCL system, quantifying the percentage of true ground displacement measurable along the satellite's LOS. The obtained C values differ depending on the acquisition orbital geometry and are lower in ascending geometry than in descending one. The C-factor values, predominantly exceeding 60%, indicate that a significant portion of the true ground displacement is measurable by the satellite.

Figure 8a and b illustrates how PS-derived ground motion data helped in refining the geomorphological interpretation of the landslide system's internal sectors. The analysis revealed that a significant portion of the slope is involved in the progressive deformation of the rock mass and that this actively deforming area is broader compared to what previous literature reported.

The ascending geometry shows significantly lower velocity ranges compared to the descending geometry. The Rubble Zone primarily exhibits negative displacement values (indicating movement towards the satellite LOS in a northwestward direction), ranging between −5 and −7.5 mm/y. Velocities up to 10 mm/y are observed at the bottom of the Active cliff face of the DCL. These negative values abruptly shift to positive (+5 mm/y) at the Main Rotational scarp. A similar trend is recorded along the Upper Block's body, though the vegetation presence reduces the PS density. Moreover, considering the lower values of the C factor in the ascending geometry, the LOS velocity information measured in the descending geometry was considered more reliable for accurately estimating the actual extent of the deforming area. In fact, the descending orbit not only is characterized by a larger PS number but also captures a broader range of displacement rates, exceeding 25 mm/y, compared to the ascending one. Displacement values range from −10 to −15 mm/y and are predominantly observed in the central portion of the Rubble Zone and the top of the Upper Block. Clusters of −15 to −25 mm/y characterize the eastern part of the Main Rotational Zone and the Rubble Zone. This heavily deforming core gradually fades towards lower displacement values through the Main and East Rotational bodies, as well as at the Upper Block's foot.

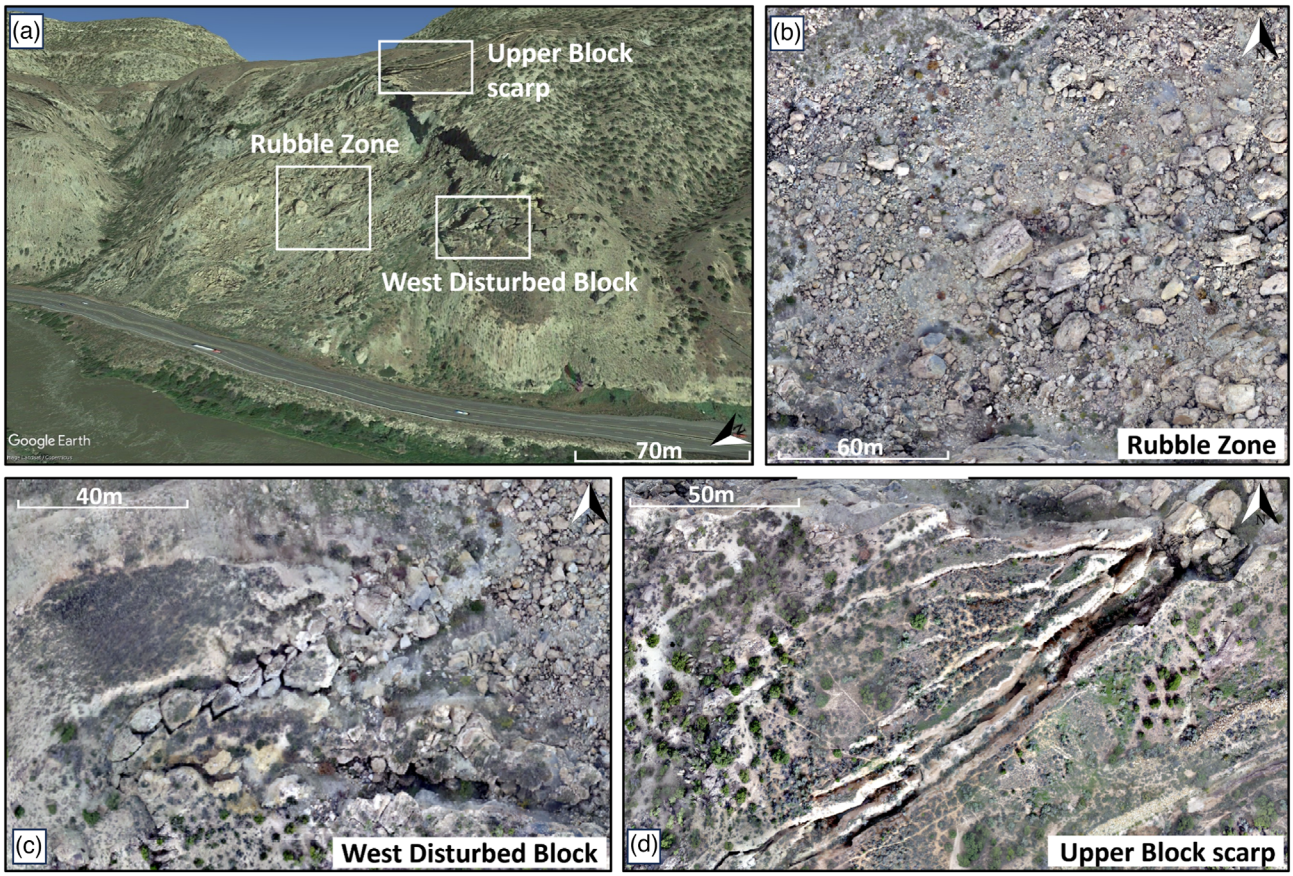

FIGURE 5 Oblique view of the DCL (panel a, image taken from GoogleEarth) and details of its surficial deposit and geomorphological features in correspondence with the rubble zone (b), west disturbed block (c) and upper block scarp (d). The latter three panels were modified after White, (2014).

The PS time series, representative of the landslide central sector's displacements and shown in Figure 8b and e, exhibits a trend without clear evidence of sudden accelerations or abrupt changes in either geometries.

The PS data was refined through post-processing to spatially distinguish the kinematics of different gravitational processes within the landslide system.

The vectorial decomposition outcomes are illustrated in Figure 9a and b. The Rubble Zone exhibits a strong vertical component (<−12.5 mm/y) with minor eastward displacement rates (up to −12.5 mm/y for some synthetic points). Similarly, the East and Main Rotational Zones show greater vertical than horizontal deformation, except for two clusters located both in the eastern and western boundary of the Main Rotational Zone, where velocities exceed −12 mm/y. The Upper Block is the only sector experiencing marked horizontal displacements, while other sectors show both vertical and horizontal displacements. By combining the decomposed multi-geometry datasets, we obtained the bidimensional vector Vt and the related Δ, expressing the connection between the landslide movement and the local topography (Figure 9c). The Δ distribution changes over the DCL, shifting from negative and null ($-5° < \Delta < 5°$) values in the Upper Block to predominantly positive values in the other sectors. Most of the DCL body exhibits a strong downward movement, with the Upper Block being the only sector displaying movements parallel to the surface topography and, in its lower part, with a bulging component of the vector Vt (Figure 9d). Moreover, examples of the Vt vector time series for each of the landslide sectors are reported in Figure 10.

The frequency distribution analysis enabled a more precise assessment of the multimodal LOS velocity distribution than previously estimated through visual analysis. Distinct PS clusters are identified for specific velocity intervals where the distribution shows significant peaks, indicating marked segmentation of process kinematics. The ascending geometry's frequency distribution is strongly peaked around zero, with a slight asymmetry towards negative velocity values, where a modest peak is located at -7 mm/y (Figure 11a). Conversely, the descending distribution shows a multimodal curve (Figure 11b), including two peaks at approximately −4 and −18 mm/y. We evaluated the Δ gradient distribution for the Rubble Zone, Upper Block and Main and East Rotational zones (Figure 11c). Figure 10c illustrates the four distinct distributions along with the averaged DCL curve. All the frequency curves are centred between 20 and 40° except for the Upper Block, which peaks around zero.

This divergence implies that the Upper Block is the only sector with plain translational movement, as its Δ values approximating zero indicate more frequent motions along the slope inclination. Different from what was reported in previous studies, along with the Main and East Rotational Zones, the Rubble Zone itself displays an evident rotational kinematic component. To discriminate the predominant failure mechanism among the full spectrum of translational to rotational kinematics, we exploited the median and skewness parameters as a measure of the Δ distributions' diversity (Figure 11d). Negative values for both parameters isolate the Upper Block in the translational domain, while purely rotational phenomena occupy the first quadrant of the diagram. Instead, the Rubble Zone and DCL, despite falling within

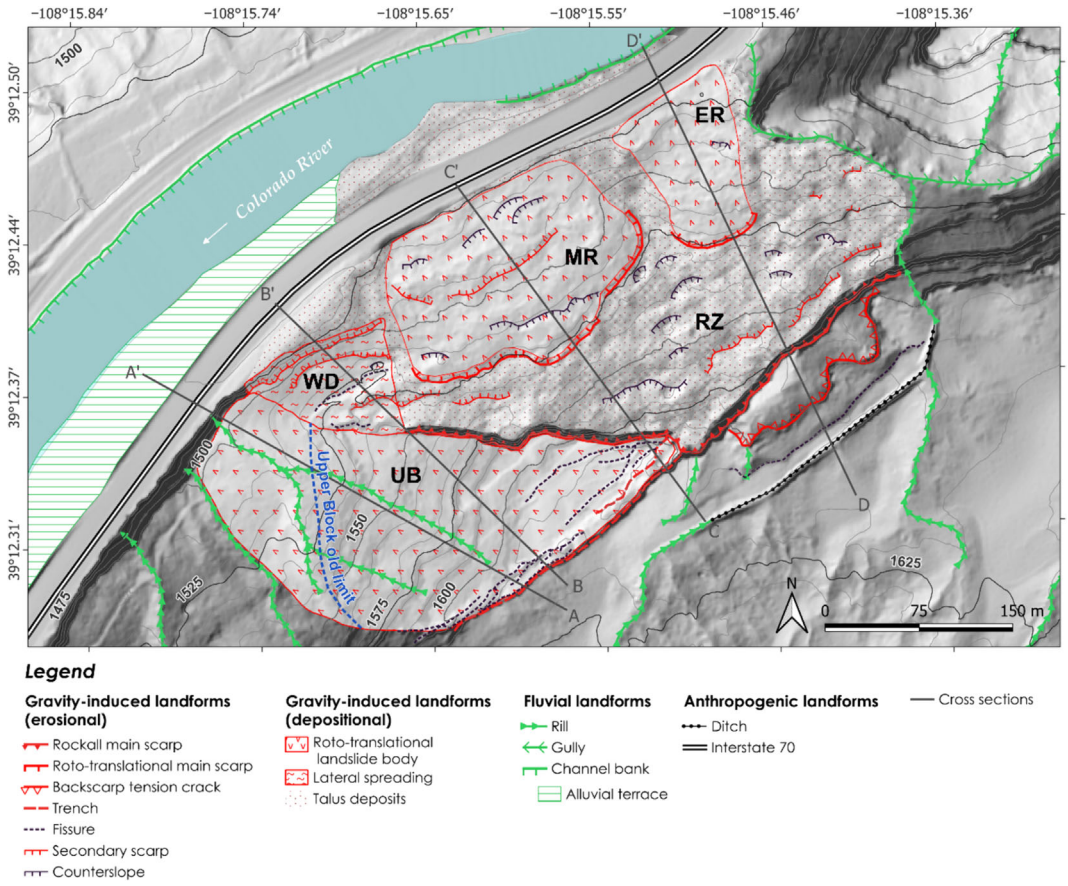

FIGURE 6 Geomorphological map of the DCL showing the revised delineation of the upper block (UB), west disturbed block (WD), Main rotational zone (MR), east rotational zone (ER) and rubble zone (RZ). The four sections shown here were used as exemplary topographic profiles for different landslide sectors to project Vt (see Section 3.2). Geodetic coordinate system (EPSG: 4326).

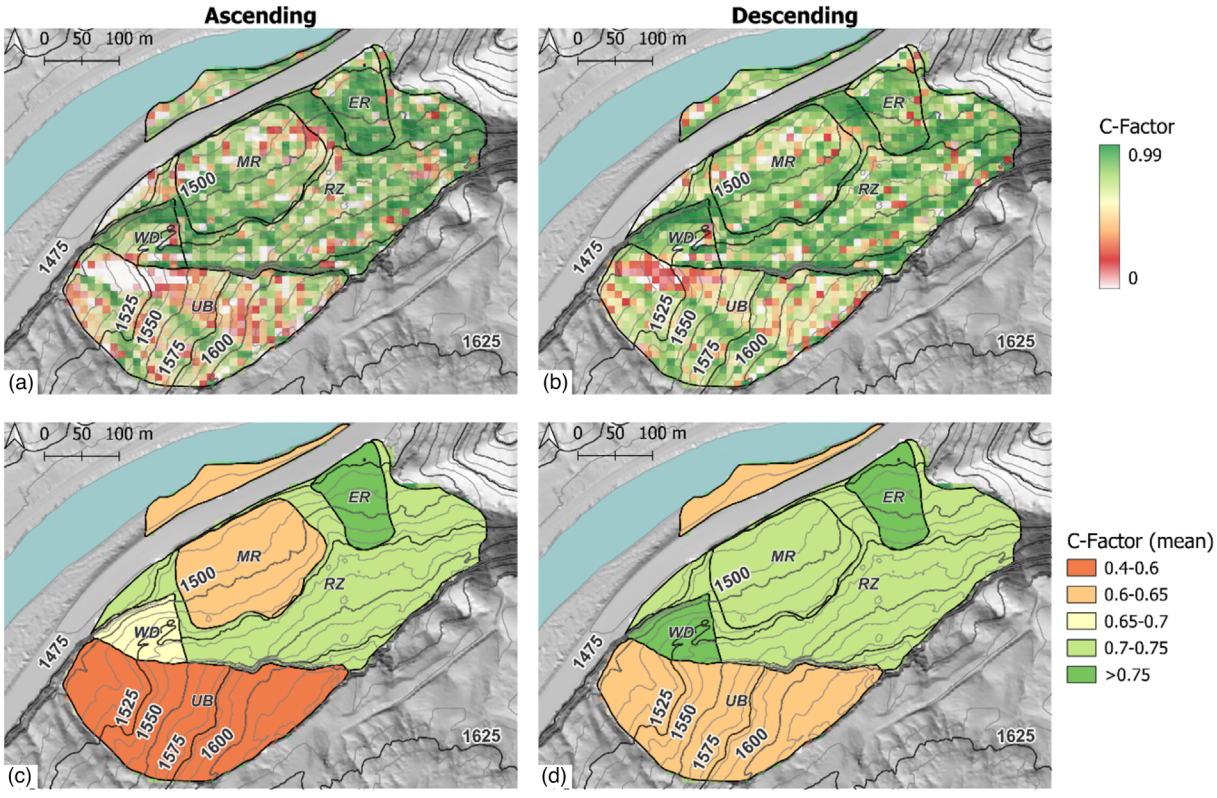

FIGURE 7 Maps showing C-factor computed for the ascending (left panels) and descending (right panels) geometries. Panels a and b show the C-factor map calculated for the entire extent of the DCL. Each landslide's sector is also coloured based on the C-factor mean (panels c and d) for the respective area.

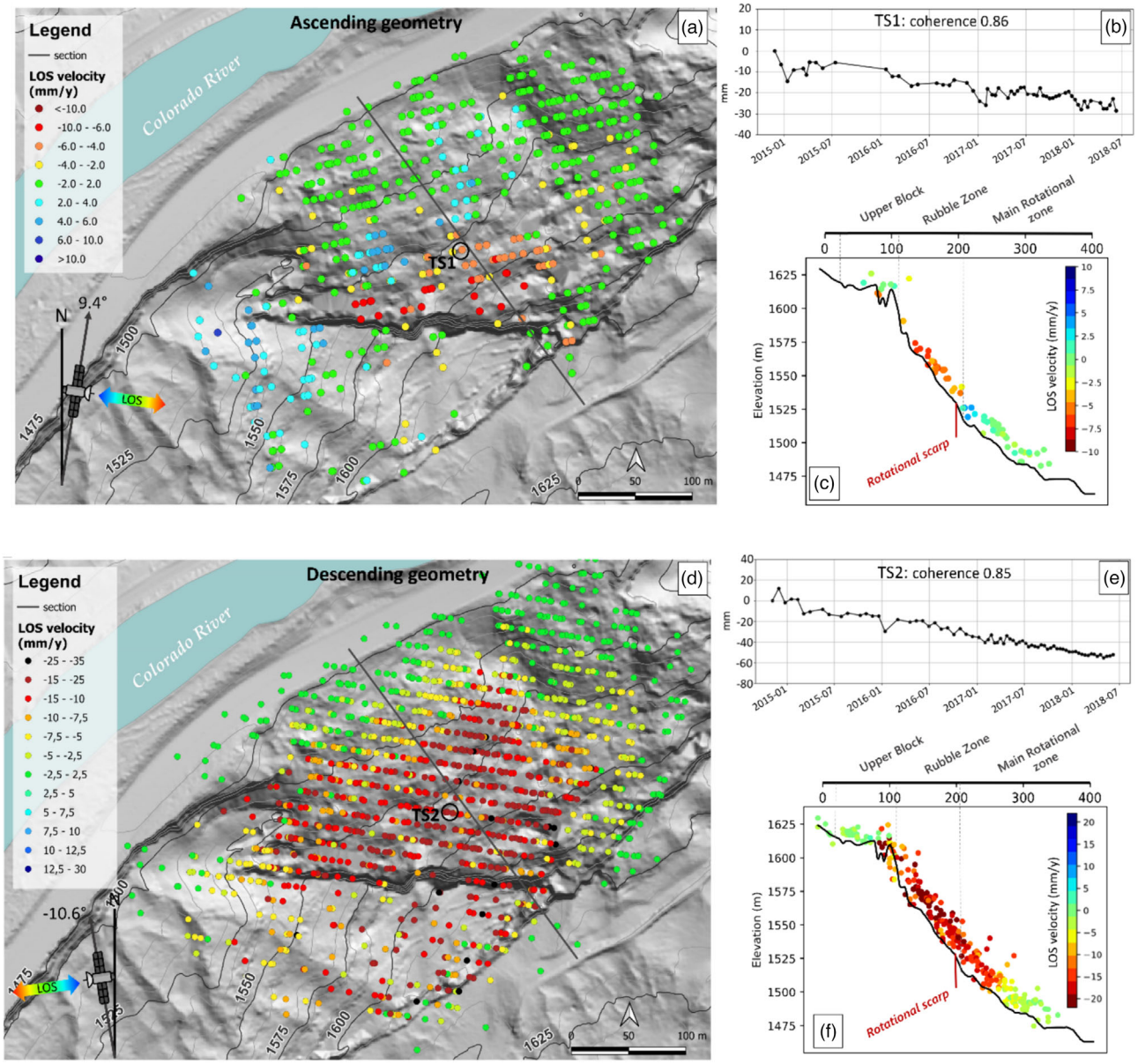

FIGURE 8 Panels a) and d) represent the PS distribution over the DCL extension for the ascending and descending geometries. Panels b) and e) report the representative time series, while panels c) and f) show the topographic cross sections along which the PS are projected. Geodetic coordinate system (EPSG: 4326).

the rotational domain, share high median values (>20°) and asymmetric curves (negative skewness).

We further examined the displacement bidimensional vector Vt for each landslide sector to visualize the differential kinematics throughout the whole landslide system. The inclination and absolute value of Vt were projected considering four 30 m-wide swath profiles crossing each landslide zone (Figure 12).

The Upper Block's synthetic PSs (Figure 12a) predominantly record along-slope movement, confirming translative displacement. The profile of Figure 12b, spanning the Upper Block to the West Disturbed Block, exhibits a bimodal Vt gradient trend, with a sharp shift at around 150 m. The upper portion preserves an along-slope (or slightly inward) orientation, typical of the Upper Block dynamics, while the lower half shows inward-dipping vectors (positive Δ). Main (Figure 12c) and East Rotational Zones (Figure 12d) display positive Δ values, strongly dipping inward in upper and central slopes, gradually decreasing at the foot where Vt becomes almost parallel to the slope.

Figure 13 shows the temporal characterization of the landslide system deformational pattern. Specifically, a-d plots refer to different system sectors and display abrupt changes (>90% probability of occurrence) and relative counting on a weekly and monthly basis for the analysed time interval (2015–2018). Clustering of such abrupt changes reveals similar-timed acceleration trends for most of the time series.

Main Rotational, East Rotational and Rubble Zones show similar trends, with displacement rate changes during December–February of 2016, 2017 and 2019, and to a lesser extent in 2015. These periods coincide with 30-year average temperatures between +4°C and −2°C, showing no clear correspondence with positive temperature anomalies of 2015, 2017 and 2018.

Conversely, the Upper Block uniquely shows abrupt changes at the end of winter (February–March) of the same years except for 2019. During these time frames, the average temperature over 30 years fluctuates between +2°C and −2°C.

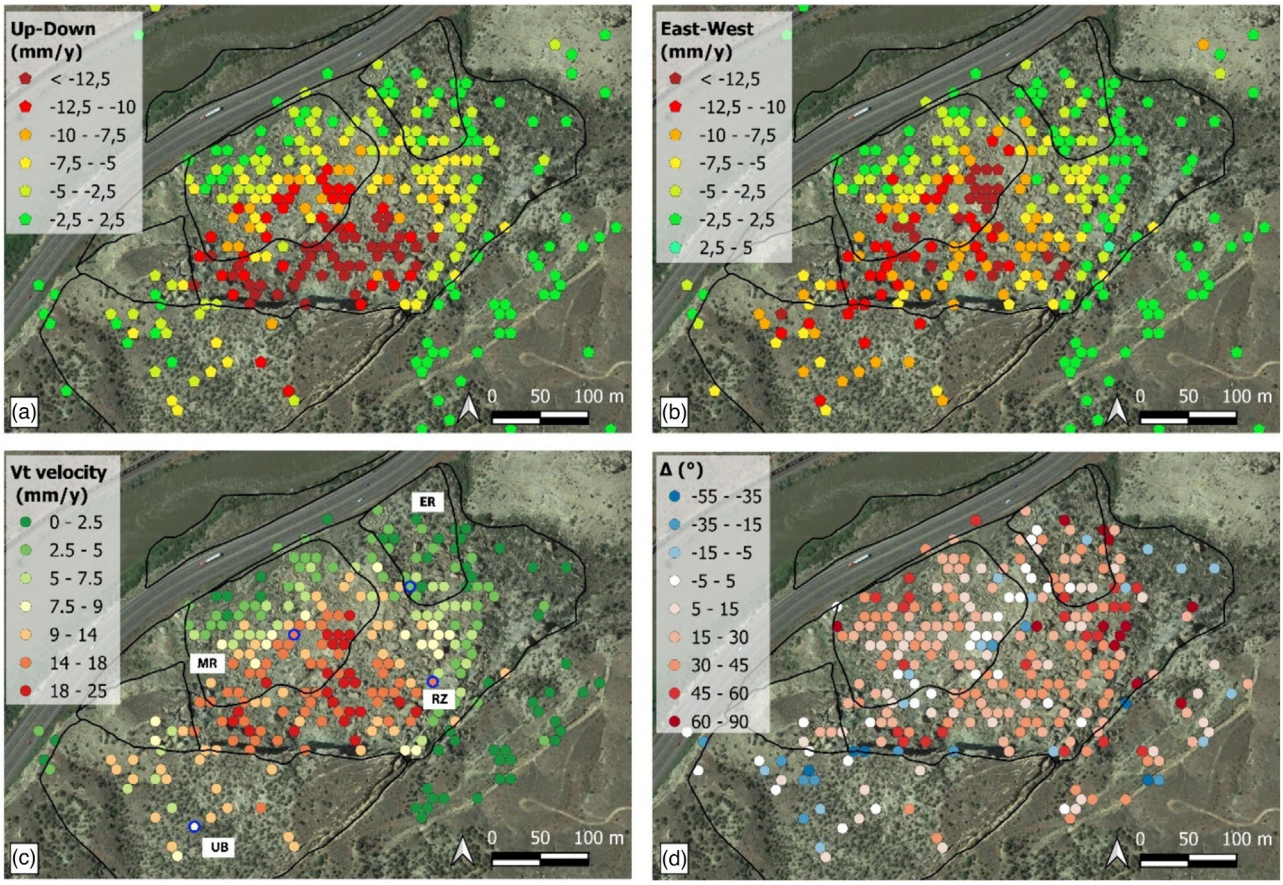

FIGURE 9 PS-InSAR velocity decomposition. a) Visualization of the decomposed velocity along the vertical direction (colours towards red shades represent subsiding movement); b) visualization of the decomposed velocity along the horizontal direction (colours towards red shades represent movement to the east, light blue to west); c) representation of vector Vt, where 4 PS are outlined in blue, as their respective time series are shown in Figure 10; d) representation of Δ.

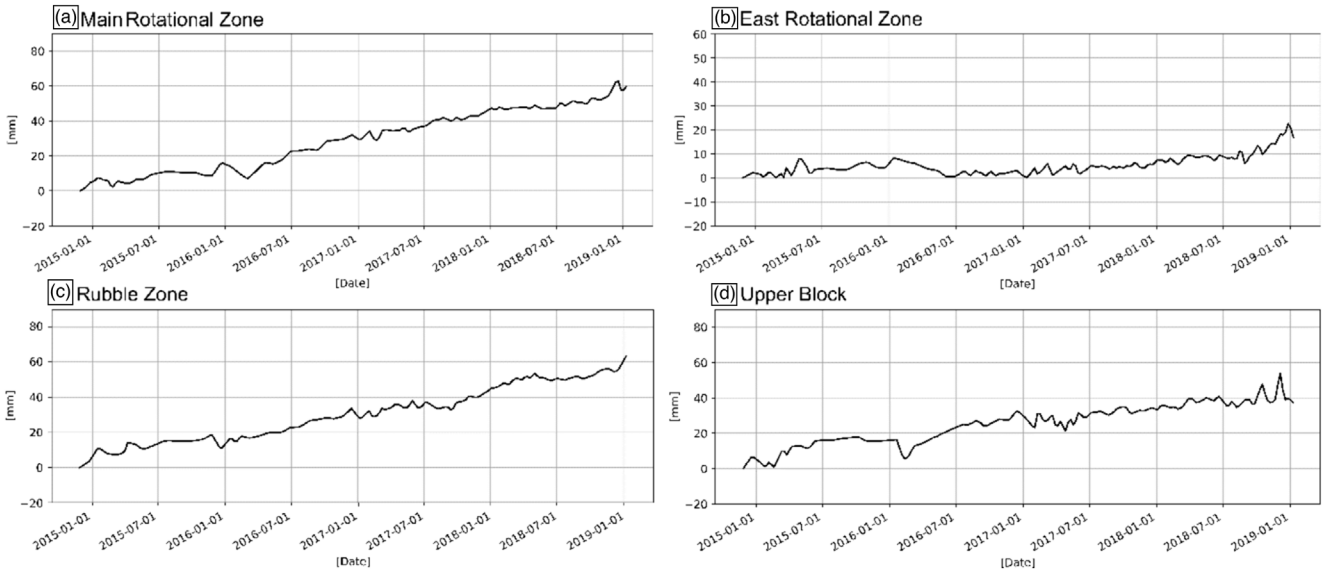

FIGURE 10 Time series of the displacement vector Vt for the landslide system sectors (the locations of the respective PS are shown in Figure 9): a) Main rotational zone; b) east rotational zone; c) rubble zone; d) upper block.

In addition, other occasional variations within the trend were recorded in correspondence with exceptionally rainy months. All sectors, especially the Upper Block, showed displacement during April–June 2015 and 2016 rainfall anomalies. Similarly, during the June–July 2017 period, significant acceleration is noticed even without monthly precipitation anomalies as those recorded in 2015 and 2016.

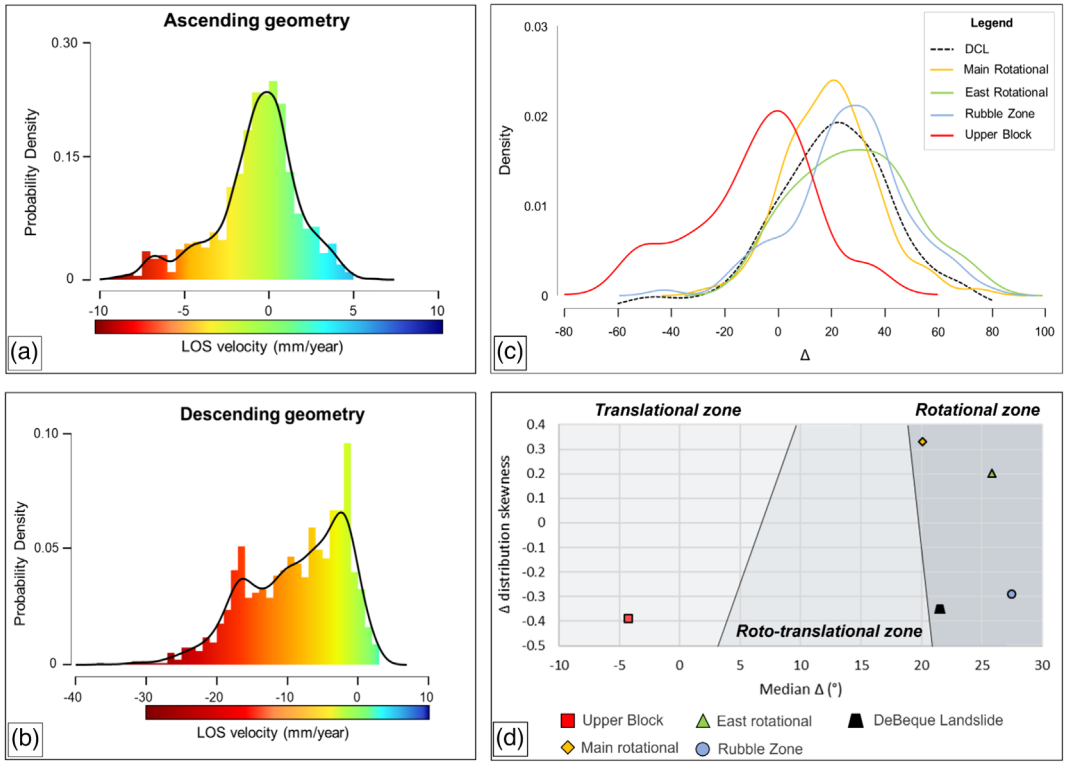

FIGURE 11 Results from the spatial post-processing analysis for the differential kinematic characterization of the DCL are shown in this picture. Panels a) and b) display the distribution of the ascending and descending LOS velocity for the whole DCL area. Panel c) Δ distribution; panel d) landslide sectors' classification based on Δ skewness and median parameters (boundaries separating translational and rotational zones based on Crippa et al., 2021).

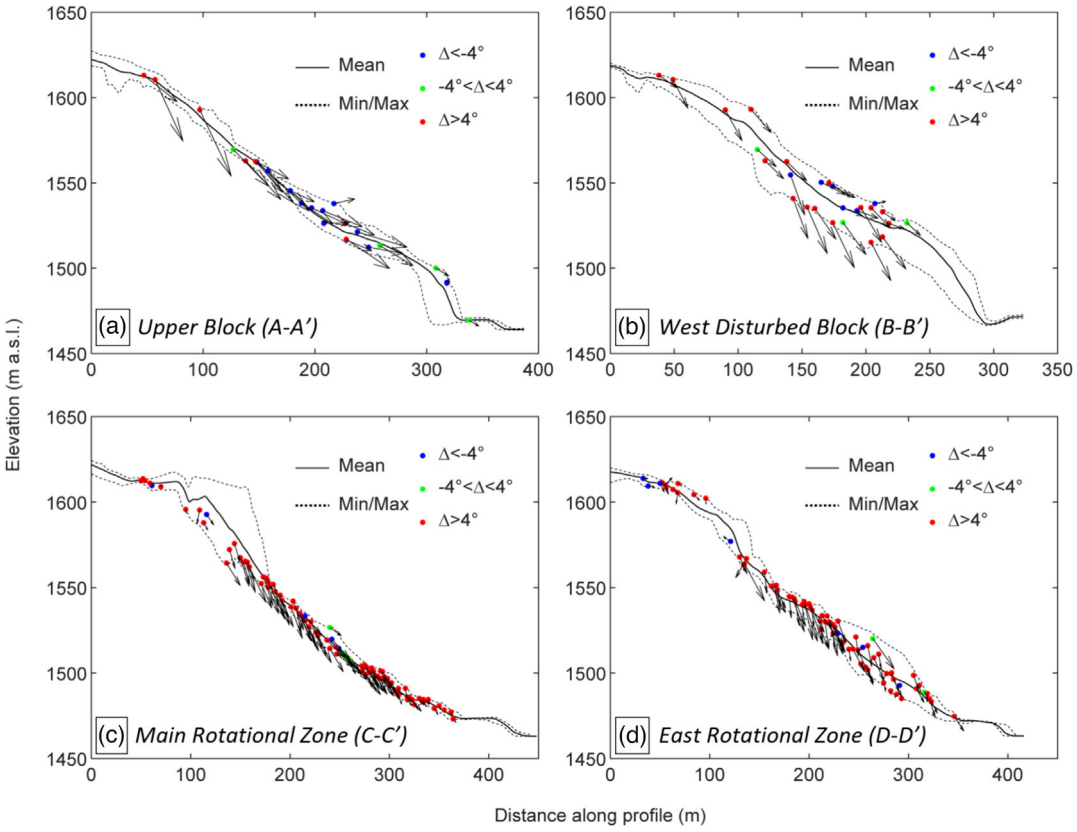

FIGURE 12 Projection of the synthetic PS along 4 different swath topographic profiles displayed in Figure 6 and intersecting: a) the upper block; b) the upper block and west disturbed block; c) the Main rotational zone; and d) the east rotational zone. For each synthetic point, its bi-dimensional vector Vt and Δ values are respectively displayed by an arrow (whose length is proportional to Vt modulus) and categorized with respect to negative (<−4°), positive (>4°) and circa null Δ values (−4° < Δ < 4°).

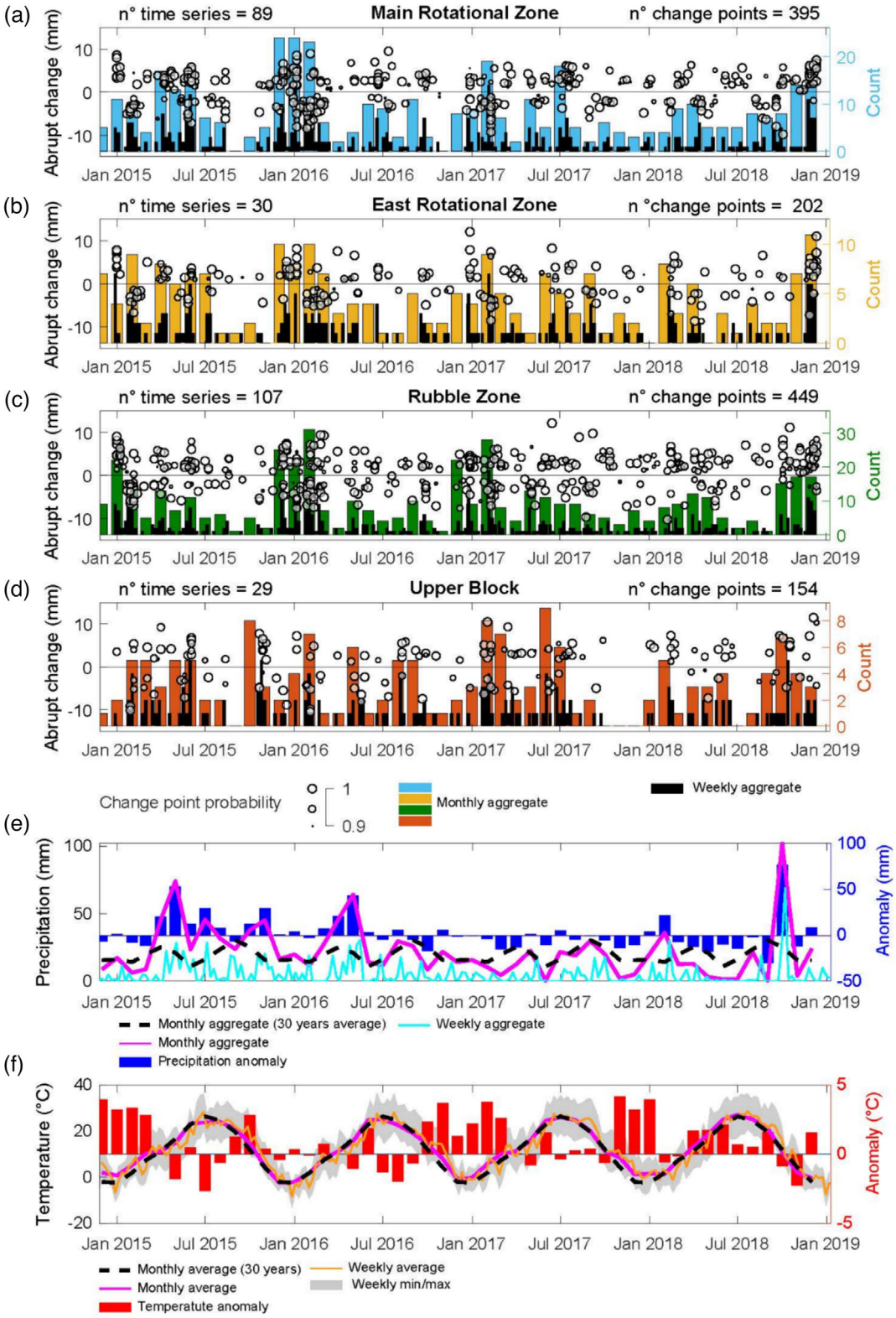

FIGURE 13 Trend change detection results for the four different sectors of the landslide system (panels a-d). For each time series, abrupt changes exceeding a 90% probability of occurrence threshold are displayed as black circles, while abrupt change counts are represented on a weekly (black bars) and monthly basis (coloured bars). Daily precipitation and temperature values are shown as weekly and monthly aggregate or average, respectively, in panel e) and panel f), along with their respective 30-year trends and related anomalies (blue and red bars).

Moreover, the Upper Block displayed abrupt changes during the October–November period of 2015 and 2018. October 2018 saw the most intense rainfalls (and, consequently, the highest recorded anomaly), followed by May 2015 and May 2016. For each of these periods, the Upper Block exhibits significant displacements, less pronounced in the other sectors.

4 | DISCUSSION

Through post-processing of the InSAR information, we identified the variability in displacement patterns characterizing different sectors of the landslide system, highlighting their intrinsic spatial heterogeneity and asynchronous responses over time to both impulsive and

prolonged external stresses. Our remote sensing approach proves valuable when field instrumentation data are unavailable or limited for ground validation, as exemplified in the presented case study. However, when feasible, integrating remote sensing data with field observations and in-situ measurements provides a more comprehensive understanding of landslide dynamics and improves the overall interpretation reliability (Guzzetti et al. 2012; Refice et al., 2019).

The satellite multi-geometry combination allowed for an accurate investigation of each cluster's displacement component along the actual movement direction rather than just the sensor's LOS. In this regard, we considered that the north–south displacement component is not visible by the SAR technique. This overcomes the limitation of one-dimensional LOS measurements, which do not accurately represent true landslide movement. Previous researchers (Aslan et al., 2020; Bianchini et al., 2013; Herrera et al., 2013; Kalia, 2018; Notti et al., 2014) attempted to address this by relating landslide displacement to local slope morphology, transforming velocity measurements from LOS to maximum slope direction (Vslope). While valuable for certain scenarios, this approach is primarily effective for characterizing purely translational kinematics and lacks generalizability to more complex movement patterns. Conversely, our approach of converting measurements into a bidimensional displacement vector Vt proved more suitable for characterizing complex movement patterns, demonstrating broader applicability and enabling the characterization of internal displacement heterogeneity from a remote sensing perspective. Moreover, to address potential limitations of SAR measurements, particularly regarding the N-S component of landslide displacement, we employed the C-factor analysis. Our findings suggest that, while some minor underestimation in LOS velocity may occur, the overall reliability of our InSAR analysis is robust, thus allowing us to proceed with post-processing analyses.

We effectively show how different dips of the displacement vector relative to slope gradient reflect the shift from translational (i.e., the Upper Block) to rotational slides (i.e., Main and East Rotational Zone). The Upper Block, the only example of a translational landslide within this system, shows Vt vectors with a marked displacement component parallel to the slope, except for the rock wedge in its upper portion, bounded by a trench and fractures. This peculiar behaviour is visible even along the B-B′ profile (Figure 12b): from an almost parallel (or at least slightly inclined) motion along the slope, the deformation direction shifts to dipping inward the slope when reaching the West Disturbed Block, where the displacement has a considerable vertical component (Figure 12b).

Moreover, our data suggests a different interpretation of the Rubble Zone kinematics compared to previous studies (White, 2005; Weidner & Walton, 2020). While authors indicate a translational movement along a 30 m deep shear zone parallel to the slope, surface displacements exhibit a marked subsiding component, discernible through the Vt projection along the cross-sections (C-C′ and D-D′). The Rubble Zone's vectors are strongly oriented inside the slope rather than parallel to it, maintaining an orientation very similar to those located within the Main and East Rotational landslides, characterized exclusively by a rotational kinematic component. For such sectors, the vectors gradually become less inclined due to the bulging effect towards the foot of the landslides.

Furthermore, we delved into the temporal aspect of the Vt vector by comparing displacement time series with meteorological and climatic factors. There seems to be a notable correlation between the temperatures during the coldest months (December–March) and the displacements, particularly in the Main, East and Rubble Zones. Conversely, the deformation response in the Upper Block aligns more closely with precipitation anomalies. This distinctive system response can be interpreted as a consequence of varying deformative evolutionary stages: the Main, East and Rubble Zones exhibit advanced evolution, while the Upper Block is still experiencing ongoing deformation. Specifically, rock mass fracturing, more pronounced in advanced evolutionary stages, plays a significant role during thermal expansion-contraction cycles that induce both the growth of pre-existing cracks and the genesis of new ones (Grechi et al., 2021; Scaringi & Loche, 2022). To substantiate this hypothesis, a more comprehensive study of the system's underground dynamics is essential.

Nevertheless, the conducted temporal analysis allowed us to draw some inferences about the activity style of the landslide system. Generally, we observed that the system shows accelerating trends primarily during winter periods. The impact of multiple cyclic actions related to thermal stress is known to have a significant effect on rock masses, especially over long periods (Grechi et al., 2021; Marmoni et al., 2020). The superimposition of freeze–thaw cycles on the rock mass facilitates the weakening of the rock, degrading the mass and acting on existing fractures (propagating and widening them) or generating new ones (Morcioni et al., 2022; Scaringi & Loche, 2022). This thermo-mechanical action was detected through Bayesian analysis of the PS time series. The effect may be further exacerbated by rapid ice melting within fissures, a result of anomalous temperatures recorded during winter periods in the investigated timeframe.

Regarding the relationship between precipitation and acceleration in deformations, the period that shows the strongest correlation is the rainy interval from April to June 2015. In this case, it was the prolonged rainfalls during this period that led to accelerations across all sectors of the DCL, rather than more limited exceptional events like those in 2016 and 2018. This aligns with observations that landslides with very deep sliding surfaces are mostly triggered by prolonged, low-intensity rainfalls (Prokešová et al., 2013; Wang et al., 2020). Moreover, considering the lithological setting of the DeBeque Canyon, where clayey and arenaceous flysch deposits are exposed, abrupt spatial variations in hydraulic conductivity led by short-range changes in material properties are likely to occur. Such a system, responding to long-term hydraulic (and thermic) fluctuations, is affected by slow but consistent alterations in material strength over long-term periods. This aligns with the high annual temperature ranges recorded in the area (Figure 1), indicating that thermal variations play a significant role in the system's long-term evolution. This can also have a significant influence on landslide dynamics, as changes in pore water pressure can potentially lead to heterogeneous kinematic responses of the different sectors (Picarelli et al., 2022; Scaringi & Loche, 2022). The analysis would have also benefited from including solid precipitation data alongside liquid precipitation records. Unfortunately, this comprehensive analysis was not feasible due to limitations in the available data, as the meteorological station in Palisade provided only a partial record of snow precipitation, which was insufficient for a robust comparison with other datasets.

It is worth noting that the Upper Block is the sector with the fewest PS. This is not likely to affect the spatial analysis, as both the upper and lower parts of the sector are covered by measurement

points. However, the relative PS time series might not be sufficient to ensure that this sector's temporal displacement pattern is clearly different from the others. The different acceleration stages recorded for the Upper Block might result from significant outliers or localized responses to external forcings, not adequately filtered due to the lack of a more robust statistical analysis possible with more PS.

5 | CONCLUSIONS

The presented results highlight the efficacy and flexibility of our methodological approach. It can be applied at different scales, from local phenomena to regional inventories, without incurring additional costs or requiring time-consuming field surveys or long-term in-situ monitoring campaigns. Assessing the internal segmentation that slow-moving landslide systems experience under persistent stress and differential deformation can lead to the identification of potential collapse scenarios of one or more sectors that are part of this system. In addition, understanding the impact of conditioning factors on each sector of the main landslide is valuable for evaluating the heterogeneous displacement pattern from a temporal perspective. Both assessments represent a critical point in the design of mitigation measures when considering the potential asynchronous reactivation of different portions of the landslide and, therefore, carefully planning solutions to be adapted to individual dynamic and temporal evolution. The combination of high-resolution topographic information and satellite data allowed us to precisely update and delimit the actual deformational extent of the entire landslide, so far partially underestimated. We presented a reproducible method that can be used in combination with in-situ measurements or as a self-stand method for the assessment of the heterogeneous spatio-temporal displacement pattern of landslide systems. Our findings demonstrate how interferometric data can discriminate between the different processes involved in the progressive destabilization of the DCL, characterized by dynamic disruptions with differential movements and seasonal acceleration timing. Specifically, we achieved precise identification of different kinematics characterizing the landslide system was accomplished through SAR-derived 2D displacement components, obtained by exploiting the satellite multi-look acquisition mode. Statistical variables associated with the 2D vector were analysed to distinguish rotational or translational components of the landslide movement solely using surface displacement measures. Furthermore, the 2D vector time series were decomposed through a Bayesian model and correlated with meteo-climatic factors (i.e., precipitation and temperature) to identify changes in the deformational trend of each sector. Main acceleration stages were found for the Rubble Zone, Main and East Rotational Zones mainly during winter periods, while the Upper Block acceleration stages seem more correlated to precipitation anomalies.

Finally, a more detailed understanding of the spatial and temporal dynamics of landslide systems lays the foundation for more accurate multi-hazard scenario studies.

AUTHOR CONTRIBUTIONS

M.Z.: conceptualization, funding acquisition, methodology, investigation, resources, writing – initial draft, writing – reviewing and editing; M.D.: conceptualization, methodology, investigation, resources, software, writing – initial draft, writing – reviewing and editing; F.T.: supervision, writing – reviewing and editing; G.S.M.: supervision, writing – reviewing and editing; P.M.: resources, supervision: writing – reviewing and editing.

ACKNOWLEDGEMENTS

This work has been possible thanks to international collaboration with the Colorado Geological Society and the Colorado Department of Transportation, who provided essential technical reports and valuable feedback for the validation of InSAR measurements. We thank Luciano Rocca for providing the initial literature research. The authors are also grateful to the Editor and two anonymous reviewers for their critical feedback on an early draft of the manuscript. Open access publishing facilitated by Sapienza University of Rome, as part of the Wiley - CRUI-CARE agreement.

DATA AVAILABILITY STATEMENT

The data that support the findings of this study are available on request from the corresponding author.

COMPETING INTEREST STATEMENT

The authors declare that they have no conflict of interest.

ORCID

Marta Zocchi https://orcid.org/0000-0002-8890-0331
Michele Delchiaro https://orcid.org/0000-0002-0843-1003

REFERENCES

Agliardi, F., Crosta, G.B. & Frattini, P. (2012) 18 slow rock-slope deformation. *Landslides: Types, Mechanisms and Modeling*, 207, 207-221. Available from: https://doi.org/10.1017/CBO9780511740367.019.

Antonielli, B., Mazzanti, P., Rocca, A., Bozzano, F. & Dei Cas, L. (2019) A-DInSAR performance for updating landslide inventory in mountain areas: an example from lombardy region (Italy). *Geosciences*, 9(9), 364. Available from: https://doi.org/10.3390/geosciences9090364.

Ardizzone, F., Cardinali, M., Galli, M., Guzzetti, F. & Reichenbach, P. (2007) Identification and mapping of recent rainfall-induced landslides using elevation data collected by airborne Lidar. *Natural Hazards and Earth System Sciences*, 7(6), 637–650. Available from: https://doi.org/10.5194/nhess-7-637-2007.

Aslan, G., Foumelis, M., Raucoules, D., De Michele, M., Bernardie, S. & Cakir, Z. (2020) Landslide mapping and monitoring using persistent scatterer interferometry (PSI) technique in the French Alps. *Remote Sensing*, 12(8), 1305. Available from: https://doi.org/10.3390/rs12081305.

Berardino, P., Fornaro, G., Lanari, R. & Sansosti, E. (2002) A new algorithm for surface deformation monitoring based on small baseline differential SAR interferograms. *IEEE Transactions on Geoscience and Remote Sensing*, 40(11), 2375–2383. Available from: https://doi.org/10.1109/TGRS.2002.803792.

Bianchini, S., Herrera, G., Mateos, R.M., Notti, D., Garcia, I., Mora, O., et al. (2013) Landslide activity maps generation by means of persistent scatterer interferometry. *Remote Sensing*, 5(12), 6198–6222. Available from: https://doi.org/10.3390/rs5126198.

Bigot-Cormier, F., Braucher, R., Bourlès, D., Guglielmi, Y., Dubar, M. & Stéphan, J.F. (2005) Chronological constraints on processes leading to large active landslides. *Earth and Planetary Science Letters*, 235(1–2), 141–150. Available from: https://doi.org/10.1016/j.epsl.2005.03.012.

Bonì, R., Bordoni, M., Vivaldi, V., Troisi, C., Tararbra, M., Lanteri, L., et al. (2020) Assessment of the Sentinel-1 based ground motion data feasibility for large scale landslide monitoring. *Landslides*, 17(10), 2287–2299. Available from: https://doi.org/10.1007/s10346-020-01433-3.

Bordoni, M., Bonì, R., Colombo, A., Lanteri, L. & Meisina, C. (2018) A methodology for ground motion area detection (GMA-D) using A-DInSAR time series in landslide investigations. *Catena*, 163, 89–110. Available from: https://doi.org/10.1016/j.catena.2017.12.013.

Bossi, G., Cavalli, M., Crema, S., Frigerio, S., Quan Luna, B., Mantovani, M., et al. (2015) Multi-temporal LiDAR-DTMs as a tool for modelling a complex landslide: a case study in the Rotolon catchment (eastern Italian Alps). *Natural Hazards and Earth System Sciences*, 15(4), 715–722. Available from: https://doi.org/10.5194/nhess-15-715-2015.

Bozzano, F., Mazzanti, P., Perissin, D., Rocca, A., De Pari, P., & Discenza, M. E. (2017). Basin scale assessment of landslides geomorphological setting by advanced InSAR analysis. *Remote Sensing*, 9(3), 267. https://doi.org/10.3390/rs9030267

Bozzano, F., Mazzanti, P., Prestininzi, A. & Scarascia Mugnozza, G. (2010) Research and development of advanced technologies for landslide hazard analysis in Italy. *Landslides*, 7(3), 381–385. Available from: https://doi.org/10.1007/s10346-010-0208-x.

Ciampalini, A., Raspini, F., Frodella, W., Bardi, F., Bianchini, S. & Moretti, S. (2016) The effectiveness of high-resolution LiDAR data combined with PSInSAR data in landslide study. *Landslides*, 13(2), 399–410. Available from: https://doi.org/10.1007/s10346-015-0663-5.

Colorado Climate Center (n.d.) *Providing information and expertise on Colorado's complex climate*. Colorado Climate Center, Fort Collins, CO. Available from: https://climate.colostate.edu (Last accessed on 19/12/2023)

Crippa, C. & Agliardi, F. (2021) Practical estimation of landslide kinematics using PSI data. *Geosciences*, 11(5), 214. Available from: https://doi.org/10.3390/geosciences11050214.

Crippa, C., Franzosi, F., Zonca, M., Manconi, A., Crosta, G.B., Dei Cas, L., et al. (2020) Unraveling spatial and temporal heterogeneities of very slow rock-slope deformations with targeted DInSAR analyses. *Remote Sensing*, 12(8), 1329. Available from: https://doi.org/10.3390/rs12081329.

Crippa, C., Valbuzzi, E., Frattini, P., Crosta, G.B., Spreafico, M.C. & Agliardi, F. (2021) Semi-automated regional classification of the style of activity of slow rock-slope deformations using PS InSAR and SqueeSAR velocity data. *Landslides*, 18(7), 2445–2463. Available from: https://doi.org/10.1007/s10346-021-01654-0.

Crosta, G.B. & Agliardi, F. (2002) How to obtain alert velocity thresholds for large rockslides. *Physics and Chemistry of the Earth, Parts a/B/C*, 27(36), 1557–1565. Available from: https://doi.org/10.1016/S1474-7065(02)00177-8.

Crosta, G.B., Agliardi, F., Rivolta, C., Alberti, S. & Dei Cas, L. (2017) Long-term evolution and early warning strategies for complex rockslides by real-time monitoring. *Landslides*, 14(5), 1615–1632. Available from: https://doi.org/10.1007/s10346-017-0817-8.

Crosta, G.B., Di Prisco, C., Frattini, P., Frigerio, G., Castellanza, R. & Agliardi, F. (2014) Chasing a complete understanding of the triggering mechanisms of a large rapidly evolving rockslide. *Landslides*, 11(5), 747–764. Available from: https://doi.org/10.1007/s10346-013-0433-1.

Crosta, G.B., Frattini, P. & Agliardi, F. (2013) Deep seated gravitational slope deformations in the European Alps. *Tectonophysics*, 605, 13–33. Available from: https://doi.org/10.1016/j.tecto.2013.04.028.

Del Ventisette, C., Casagli, N., Fortuny-Guasch, J. & Tarchi, D. (2012) Ruinon landslide (Valfurva, Italy) activity in relation to rainfall by means of GBInSAR monitoring. *Landslides*, 9(4), 497–509. Available from: https://doi.org/10.1007/s10346-011-0307-3.

Delchiaro, M., Della Seta, M., Martino, S., Dehbozorgi, M. & Nozaem, R. (2019) Reconstruction of river valley evolution before and after the emplacement of the giant Seymareh rock avalanche (Zagros Mts., Iran). Earth surface. *Dynamics (Pembroke, Ont.)*, 7(4), 929–947. Available from: https://doi.org/10.5194/esurf-7-929-2019.

Delchiaro, M., Della Seta, M., Martino, S., Moumeni, M., Nozaem, R., Marmoni, G. M., & Esposito, C. (2024). The role of long-term preparatory factors in mass rock creep deforming slopes: insights from the Zagros Mts. Belt (Iran). Landslides, 1-21. https://doi.org/10.1007/s10346-024-02252-6

Delchiaro, M., Della Seta, M., Martino, S., Nozaem, R. & Moumeni, M. (2023) Tectonic deformation and landscape evolution inducing mass rock creep driven landslides: the Loumar case-study (Zagros fold and Thrust Belt, Iran). *Tectonophysics*, 846, 229655. Available from: https://doi.org/10.1016/j.tecto.2022.229655.

Della Seta, M., Esposito, C., Marmoni, G. M., Martino, S., Scarascia Mugnozza, G., & Troiani, F. (2017). Morpho-structural evolution of the valley-slope systems and related implications on slope-scale gravitational processes: New results from the Mt. Genzana case history (Central Apennines, Italy). *Geomorphology*, 289, 60–77. https://doi.org/10.1016/j.geomorph.2016.07.003

Di Martire, D., Paci, M., Confuorto, P., Costabile, S., Guastaferro, F., Verta, A., et al. (2017) A nation-wide system for landslide mapping and risk management in Italy: the second not-ordinary plan of environmental remote sensing. *International Journal of Applied Earth Observation and Geoinformation*, 63, 143–157. Available from: https://doi.org/10.1016/j.jag.2017.07.018.

Dong, J., Zhang, L., Li, M., Yu, Y., Liao, M., Gong, J., et al. (2018) Measuring precursory movements of the recent Xinmo landslide in Mao County, China with Sentinel-1 and ALOS-2 PALSAR-2 datasets. *Landslides*, 15(1), 135–144. Available from: https://doi.org/10.1007/s10346-017-0914-8.

Dong, Y., Liao, Z., Wang, J., Liu, Q. & Cui, L. (2023) Potential failure patterns of a large landslide complex in the three gorges reservoir area. *Bulletin of Engineering Geology and the Environment*, 82(1), 41. Available from: https://doi.org/10.1007/s10064-022-03062-7.

El Bedoui, S., Guglielmi, Y., Lebourg, T. & Pérez, J.L. (2009) Deep-seated failure propagation in a fractured rock slope over 10,000 years: the La Clapière slope, the south-eastern French Alps. *Geomorphology*, 105(3–4), 232–238. Available from: https://doi.org/10.1016/j.geomorph.2008.09.025.

Eriksen, H.Ø., Lauknes, T.R., Larsen, Y., Corner, G.D., Bergh, S.G., Dehls, J., et al. (2017) Visualizing and interpreting surface displacement patterns on unstable slopes using multi-geometry satellite SAR interferometry (2D InSAR). *Remote Sensing of Environment*, 191, 297–312. Available from: https://doi.org/10.1016/j.rse.2016.12.024.

Ferretti, A., Prati, C., Rocca, F. (2000). Nonlinear subsidence rate estimation using permanent scatterers in differential SAR interferometry. *IEEE Transactions on Geoscience and Remote Sensing*, 38(5), 2202–2212. https://doi.org/10.1109/36.868878

Ferretti, A., Prati, C., & Rocca, F. (2001). Permanent scatterers in SAR interferometry. *IEEE Transactions on Geoscience and Remote Sensing*, 39(1), 8–20. https://doi.org/10.1109/36.898661

Fick, S.E. and R.J. Hijmans, 2017. WorldClim 2: new 1km spatial resolution climate surfaces for global land areas. *International Journal of Climatology* 37 (12): 4302-4315. Available at https://www.worldclim.org/data/worldclim21.html (last accessed on 19/12/2023).

Ficklin, D.L., Stewart, I.T. & Maurer, E.P. (2013) Climate change impacts on streamflow and subbasin-scale hydrology in the upper Colorado River basin. *PLoS ONE*, 8(8), e71297. Available from: https://doi.org/10.1371/journal.pone.0071297.

Frattini, P., Crosta, G.B. & Allievi, J. (2013) Damage to buildings in large slope rock instabilities monitored with the PSInSAR™ technique. *Remote Sensing*, 5(10), 4753–4773. Available from: https://doi.org/10.3390/rs5104753.

Frattini, P., Crosta, G.B., Rossini, M. & Allievi, J. (2018) Activity and kinematic behaviour of deep-seated landslides from PS-InSAR displacement rate measurements. *Landslides*, 15(6), 1053–1070. Available from: https://doi.org/10.1007/s10346-017-0940-6.

Gaffney, S.P., White, J.L. & Ellis, W.L. (2002, October) Instrumentation of the DeBeque Canyon landslide at Interstate 70 in west central Colorado. In: *In abstracts with programs*, Vol. 34, No. 6. Geological Society of America, Reston, VA, p. 48.

Gischig, V., Amann, F., Moore, J.R., Loew, S., Eisenbeiss, H. & Stempfhuber, W. (2011) Composite rock slope kinematics at the current Randa instability, Switzerland, based on remote sensing and numerical modeling. *Engineering Geology*, 118(1–2), 37–53. Available from: https://doi.org/10.1016/j.enggeo.2010.11.006.

Glenn, N.F., Streutker, D.R., Chadwick, D.J., Thackray, G.D. & Dorsch, S.J. (2006) Analysis of LiDAR-derived topographic information for characterizing and differentiating landslide morphology and activity.

Geomorphology, 73(1–2), 131–148. Available from: https://doi.org/10.1016/j.geomorph.2005.07.006.

Google Earth Pro, v.7.3.6.9345, (2016). 39°12′23.02"N, 108°15′33.81"W, elevation 1536m.

Grechi, G., Fiorucci, M., Marmoni, G.M. & Martino, S. (2021) 3D thermal monitoring of jointed rock masses through infrared thermography and photogrammetry. *Remote Sensing*, 13(5), 957. Available from: https://doi.org/10.3390/rs13050957.

Grøneng, G., Christiansen, H.H., Nilsen, B. & Blikra, L.H. (2011) Meteorological effects on seasonal displacements of the Åknes rockslide, western Norway. *Landslides*, 8(1), 1–15. Available from: https://doi.org/10.1007/s10346-010-0224-x.

Guzzetti, F., Mondini, A.C., Cardinali, M., Fiorucci, F., Santangelo, M. & Chang, K.T. (2012) Landslide inventory maps: new tools for an old problem. *Earth-Science Reviews*, 112(1–2), 42–66. Available from: https://doi.org/10.1016/j.earscirev.2012.02.001.

Herrera, G., Gutiérrez, F., García-Davalillo, J.C., Guerrero, J., Notti, D., Galve, J.P., et al. (2013) Multi-sensor advanced DInSAR monitoring of very slow landslides: the Tena Valley case study (central Spanish Pyrenees). *Remote Sensing of Environment*, 128, 31–43. Available from: https://doi.org/10.1016/j.rse.2012.09.020.

Herrera, G., Mateos, R.M., García-Davalillo, J.C., Grandjean, G., Poyiadji, E., Maftei, R., et al. (2018) Landslide databases in the geological surveys of Europe. *Landslides*, 15(2), 359–379. Available from: https://doi.org/10.1007/s10346-017-0902-z.

Hettinger, R. D., & Kirschbaum, M. A. (2002). Stratigraphy of the Upper Cretaceous Mancos Shale (upper part) and Mesaverde Group in the southern part of the Uinta and Piceance basins, Utah and Colorado (pp. 1–16). US Geological Survey.

Ibsen, M.L. & Casagli, N. (2004) Rainfall patterns and related landslide incidence in the Porretta-Vergato region, Italy. *Landslides*, 1(2), 143–150. Available from: https://doi.org/10.1007/s10346-004-0018-0.

Jaboyedoff, M., Oppikofer, T., Abellán, A., Derron, M.H., Loye, A., Metzger, R., et al. (2012) Use of LIDAR in landslide investigations: a review. *Natural Hazards*, 61(1), 5–28. Available from: https://doi.org/10.1007/s11069-010-9634-2.

Jiang, B., Liang, S., Wang, J. & Xiao, Z. (2010) Modeling MODIS LAI time series using three statistical methods. *Remote Sensing of Environment*, 114(7), 1432–1444. Available from: https://doi.org/10.1016/j.rse.2010.01.026.

Kalia, A.C. (2018) Classification of landslide activity on a regional scale using persistent scatterer interferometry at the Moselle valley (Germany). *Remote Sensing*, 10(12), 1880. Available from: https://doi.org/10.3390/rs10121880.

Kampes, B. M. (2006). *Radar interferometry* (Vol. 12). Dordrecht, The Netherlands: Springer.

Kasai, M., Ikeda, M., Asahina, T. & Fujisawa, K. (2009) LiDAR-derived DEM evaluation of deep-seated landslides in a steep and rocky region of Japan. *Geomorphology*, 113(1–2), 57–69. Available from: https://doi.org/10.1016/j.geomorph.2009.06.004.

Kopytkovskiy, M., Geza, M. & McCray, J.E. (2015) Climate-change impacts on water resources and hydropower potential in the upper Colorado River basin. *Journal of Hydrology: Regional Studies*, 3, 473–493. Available from: https://doi.org/10.1016/j.ejrh.2015.02.014.

Lopez Saez, J., Corona, C., Stoffel, M., Astrade, L., Berger, F. & Malet, J.P. (2012) Dendrogeomorphic reconstruction of past landslide reactivation with seasonal precision: the bois noir landslide, southeast French Alps. *Landslides*, 9(2), 189–203. Available from: https://doi.org/10.1007/s10346-011-0284-6.

Marmoni, G. M., Fiorucci, M., Grechi, G., & Martino, S. (2020). Modelling of thermo-mechanical effects in a rock quarry wall induced by near-surface temperature fluctuations. *International Journal of Rock Mechanics and Mining Sciences*, 134, 104440. https://doi.org/10.1016/j.ijrmms.2020.104440

Marmoni, G.M., Martino, S., Censi, M., Menichetti, M., Piacentini, D., Mugnozza, G.S., et al. (2023) Transition from rock mass creep to progressive failure for rockslide initiation at Mt. Conero (Italy). *Geomorphology*, 108750, 108750. Available from: https://doi.org/10.1016/j.geomorph.2023.108750.

Mazzanti, P., Antonielli, B., Sciortino, A., Scancella, S. & Bozzano, F. (2021) Tracking deformation processes at the Legnica Glogow Copper District (Poland) by satellite InSAR—II: Żelazny Most tailings dam. *Land*, 10(6), 654. Available from: https://doi.org/10.3390/land10060654.

Mazzanti, P., Bozzano, F., Cipriani, I. & Prestininzi, A. (2015) New insights into the temporal prediction of landslides by a terrestrial SAR interferometry monitoring case study. *Landslides*, 12(1), 55–68. Available from: https://doi.org/10.1007/s10346-014-0469-x.

Morcioni, A., Apuani, T. & Cecinato, F. (2022) The role of temperature in the stress–strain evolution of Alpine rock-slopes: thermo-mechanical modelling of the Cimaganda rockslide. *Rock Mechanics and Rock Engineering*, 55(4), 2149–2172. Available from: https://doi.org/10.1007/s00603-022-02786-y.

Moretto, S., Bozzano, F. & Mazzanti, P. (2021) The role of satellite InSAR for landslide forecasting: limitations and openings. *Remote Sensing*, 13(18), 3735. Available from: https://doi.org/10.3390/rs13183735.

Nishii, R., Matsuoka, N., Daimaru, H. & Yasuda, M. (2013) Precursors and triggers of an alpine rockslide in Japan: the 2004 partial collapse during a snow-melting period. *Landslides*, 10(1), 75–82. Available from: https://doi.org/10.1007/s10346-012-0353-5.

Notti, D., Herrera, G., Bianchini, S., Meisina, C., García-Davalillo, J.C. & Zucca, F. (2014) A methodology for improving landslide PSI data analysis. *International Journal of Remote Sensing*, 35(6), 2186–2214. Available from: https://doi.org/10.1080/01431161.2014.889864.

Perissin, D., Wang, Z., & Wang, T. (2011). The SARPROZ InSAR tool for urban subsidence/manmade structure stability monitoring in China. proceedings of the ISRSE, Sidney, Australia, 1015.

Picarelli, L., Di Maio, C., Tommasi, P., Urciuoli, G. & Comegna, L. (2022) Pore water pressure measuring and modeling in stiff clays and clayey flysch deposits: a challenging problem. *Engineering Geology*, 296, 106442. Available from: https://doi.org/10.1016/j.enggeo.2021.106442.

Popescu, M.E. (2002, July) Landslide causal factors and landslide remediatial options. In: *In 3rd international conference on landslides, slope stability and safety of infra-structures*. CI-Premier PTE LTD,Singapore, pp. 61–81.

Preisig, G., Eberhardt, E., Smithyman, M., Preh, A. & Bonzanigo, L. (2016) Hydromechanical rock mass fatigue in deep-seated landslides accompanying seasonal variations in pore pressures. *Rock Mechanics and Rock Engineering*, 49(6), 2333–2351. Available from: https://doi.org/10.1007/s00603-016-0912-5.

Prokešová, R., Medveďová, A., Tábořík, P. & Snopková, Z. (2013) Towards hydrological triggering mechanisms of large deep-seated landslides. *Landslides*, 10(3), 239–254. Available from: https://doi.org/10.1007/s10346-012-0330-z.

Raspini, F., Bardi, F., Bianchini, S., Ciampalini, A., Del Ventisette, C., Farina, P., et al. (2017) The contribution of satellite SAR-derived displacement measurements in landslide risk management practices. *Natural Hazards*, 86(1), 327–351. Available from: https://doi.org/10.1007/s11069-016-2691-4.

Refice, A., Spalluto, L., Bovenga, F., Fiore, A., Miccoli, M.N., Muzzicato, P., et al. (2019) Integration of persistent scatterer interferometry and ground data for landslide monitoring: the Pianello landslide (Bovino, southern Italy). *Landslides*, 16(3), 447–468. Available from: https://doi.org/10.1007/s10346-018-01124-0.

Reyes-Carmona, C., Galve, J.P., Pérez-Peña, J.V., Moreno-Sánchez, M., Alfonso-Jorde, D., Ballesteros, D., et al. (2023) Improving landslide inventories by combining satellite interferometry and landscape analysis: the case of Sierra Nevada (southern Spain). *Landslides*, 1-21(9), 1815–1835. Available from: https://doi.org/10.1007/s10346-023-02071-1.

Riva, F., Agliardi, F., Amitrano, D. & Crosta, G.B. (2018) Damage-based time-dependent modeling of paraglacial to postglacial progressive failure of large rock slopes. *Journal of Geophysical Research: Earth Surface*, 123(1), 124–141. Available from: https://doi.org/10.1002/2017JF004423.

Scaringi, G., & Loche, M. (2022). A thermo-hydro-mechanical approach to soil slope stability under climate change. *Geomorphology*, 401, 108108. https://doi.org/10.1016/j.geomorph.2022.108108

Scheevel, C. R., Baum, R. L., Mirus, B. B., & Smith, J. B. (2017). Precipitation thresholds for landslide occurrence near Seattle, Mukilteo, and Everett, Washington (No. 2017–1039). US Geological Survey. https://doi.org/10.3133/ofr20171039

Singhroy, V. & Molch, K. (2004) Characterizing and monitoring rockslides from SAR techniques. *Advances in Space Research*, 33(3), 290–295. Available from: https://doi.org/10.1016/S0273-1177(03)00470-8.

Steger, S., Moreno, M., Crespi, A., Zellner, P.J., Gariano, S.L., Brunetti, M.T., et al. (2022) Deciphering seasonal effects of triggering and preparatory precipitation for improved shallow landslide prediction using generalized additive mixed models. *Natural Hazards and Earth System Sciences Discussions*, 2022(4), 1–38. Available from: https://doi.org/10.5194/nhess-23-1483-2023.

Tarchi, D., Casagli, N., Moretti, S., Leva, D. & Sieber, A.J. (2003) Monitoring landslide displacements by using ground-based synthetic aperture radar interferometry: application to the Ruinon landslide in the Italian Alps. Journal of geophysical research: solid. *Earth*, 108(B8), 2387. Available from: https://doi.org/10.1029/2002JB002204.

Tofani, V., Raspini, F., Catani, F. & Casagli, N. (2013) Persistent Scatterer interferometry (PSI) technique for landslide characterization and monitoring. *Remote Sensing*, 5(3), 1045–1065. Available from: https://doi.org/10.3390/rs5031045.

U.S. Geological Survey, 2019, 3D Elevation Program 1-Meter Resolution Digital Elevation Model (published 20200606), accessed August 30, 2023 at URL https://www.usgs.gov/the-national-map-data-delivery

Valiante, M., Bozzano, F. & Guida, D. (2016) The Sant'Andrea-Molinello landslide system (Mt. Pruno, Roscigno, Italy). *Rendiconti Online Della Società Geologica Italiana*, 41, 214–217. Available from: https://doi.org/10.3301/ROL.2016.132.

Valiante, M., Guida, D., Della Seta, M. & Bozzano, F. (2021) A spatiotemporal object-oriented data model for landslides (LOOM). *Landslides*, 18(4), 1231–1244. Available from: https://doi.org/10.1007/s10346-020-01591-4.

Verbesselt, J., Hyndman, R., Zeileis, A. & Culvenor, D. (2010) Phenological change detection while accounting for abrupt and gradual trends in satellite image time series. *Remote Sensing of Environment*, 114(12), 2970–2980. Available from: https://doi.org/10.1016/j.rse.2010.08.003.

Vick, L.M., Böhme, M., Rouyet, L., Bergh, S.G., Corner, G.D. & Lauknes, T.R. (2020) Structurally controlled rock slope deformation in northern Norway. *Landslides*, 17(8), 1745–1776. Available from: https://doi.org/10.1007/s10346-020-01421-7.

Wang, J., Xiao, L., Zhang, J. & Zhu, Y. (2020) Deformation characteristics and failure mechanisms of a rainfall-induced complex landslide in Wanzhou County, three gorges reservoir, China. *Landslides*, 17(2), 419–431. Available from: https://doi.org/10.1007/s10346-019-01317-1.

Wasowski, J. & Bovenga, F. (2014) Investigating landslides and unstable slopes with satellite multi temporal interferometry: current issues and future perspectives. *Engineering Geology*, 174, 103–138. Available from: https://doi.org/10.1016/j.enggeo.2014.03.003.

Weidner, L. & Walton, G. (2020) Monitoring and modeling of the DeBeque Canyon landslide complex in three dimensions. In: *ARMA US rock mechanics/Geomechanics symposium*. ARMA, p.2020.

White, J.L. (2000) Photogrammetric analysis of Debeque Canyon Landslide from 1950 to present, Mesa County, Colorado. In: *Colorado geological survey technical report*.

White, J.L. (2005) The Debeque Canyon landslide at Interstate 70, Mesa County, West-central Colorado. In: *Rocky Mountain section, Geological Society of America, field trip guidebook (2005)*, pp. 1–8.

White, J.L. (2014) Annual Report of Instrumentation Monitoring Results from the DeBeque Canyon Landslide, Interstate 70, milepost 51. In: *DeBeque canyon landslide monitoring, 2013 annual report*. Colorado Geological Survey, Golden, CO.

White, J.L., Ellis, W.L., Higgins, J.D., Dessenberger, N.C., Gaffney, S. & Coe, J.A. (2003) Geology, instrumentation, and movement history of the DeBeque canyon landslide, Mesa County, west-Central Colorado. Engineering geology in Colorado: contributions, trends, and case histories: Association of Engineering Geologists Special. *Publication*, 14.

Xu, Q., Guo, C., Dong, X., Li, W., Lu, H., Fu, H., et al. (2021) Mapping and characterizing displacements of landslides with InSAR and airborne LiDAR technologies: a case study of danba county, Southwest China. *Remote Sensing*, 13(21), 4234. Available from: https://doi.org/10.3390/rs13214234.

Zepner, L., Karrasch, P., Wiemann, F. & Bernard, L. (2020) ClimateCharts.Net – an interactive climate analysis web platform. *International Journal of Digital Earth*, 14(3), 338–356. Available from: https://doi.org/10.1080/17538947.2020.1829112. Accessed 29 August 2023.

Zhao, K., Wulder, M.A., Hu, T., Bright, R., Wu, Q., Qin, H., et al. (2019) Detecting change-point, trend, and seasonality in satellite time series data to track abrupt changes and nonlinear dynamics: a Bayesian ensemble algorithm. *Remote Sensing of Environment*, 232, 111181. Available from: https://doi.org/10.1016/j.rse.2019.04.034.

How to cite this article: Zocchi, M., Delchiaro, M., Troiani, F., Scarascia Mugnozza, G. & Mazzanti, P. (2024) PS-InSAR post-processing for assessing the spatio-temporal differential kinematics of complex landslide systems: A case study of DeBeque Canyon Landslide (Colorado, USA). *Earth Surface Processes and Landforms*, 1–19. Available from: https://doi.org/10.1002/esp.6002